ThesisTitle

by

Daniel C. Cole

Other Degrees

A thesis submitted to the

Faculty of the Graduate School of the

University of Colorado in partial fulfillment

of the requirements for the degree of

Doctor of Philosophy

Physics Physics

2018

This thesis entitled:
ThesisTitle
written by Daniel C. Cole
has been approved for the Physics Physics

Reader1

Reader2

Date

The final copy of this thesis has been examined by the signatories, and we find that both the content and the form meet acceptable presentation standards of scholarly work in the above mentioned discipline.

Cole, Daniel C. (Ph.D., Physics)

ThesisTitle

Thesis directed by Dr. Scott A. Diddams

Optical frequency combs have revolutionized precision metrology by enabling measurements of optical frequencies, with implications both for fundamental scientific questions and for applications such as fast, broadband spectroscopy. In this thesis, I describe the development of comb generation platforms with smaller footprints and higher repetition rates, with the ultimate goal of bringing frequency combs to new applications in a chip-integrated package. I present two new types of frequency combs: electro-optic modulation (EOM) combs and Kerr-microresonator-based frequency combs (microcombs). First I describe the EOM comb scheme and, in particular, techniques for mitigating noise in the comb generation process, and I present the results of a proof-of-principle metrology experiment and some possible applications. Then I discuss developments in microcomb technology. I present novel 'soliton crystal' states, which have highly structured 'fingerprint' optical spectra that correspond to ordered pulse trains exhibiting crystallographic defects. These pulse trains arise through interaction of the solitons with avoided mode-crossings in the resonator spectrum. Next, I describe the direct and deterministic generation of single microresonator solitons using a phase-modulated pump laser. This technique removes the dependence on initial conditions that was formerly a universal feature of these experiments, presenting a solution to a significant technical barrier to the practical application of microcombs. I also discuss generation of Kerr combs in the Fabry-Perot (FP) geometry. I introduce a nonlinear partial differential equation describing dynamics in an FP cavity and discuss the differences between the FP geometry and the ring cavity, which is the geometry used in previous Kerr-comb experiments. Finally, I discuss a technique for reducing the repetition rate of a high-repetition-rate frequency comb, which will be a necessary post-processing step for some applications. I conclude with a discussion of avenues for future research, including the chip-integration of Fabry-Perot Kerr resonators and the use of band-engineered photonic crystal cavities to further simplify soliton generation.

Acknowledgements

The work in this thesis would not have been possible...

- Acknowledgement line 1
- Acknowledgement line 2

Contents

Figures

Chapter 1

Introduction

The invention of the optical frequency comb two decades ago provided a revolution in precision measurement by dramatically improving the resolution with which we can conveniently measure time [**Diddams2000**, **Jones2000**, 1–3]. This revolution came about through the development of a simple scheme (that required markedly *less* simple advancements in capabilities in nonlinear optics[4]) by which the hundreds-of-terahertz-scale optical frequencies of a mode-locked laser could be effectively measured by electronics with bandwidth limitations on the gigahertz scale. Optical frequency combs have played an integral part in experiments and applications in contexts ranging from record-setting optical clocks, systems for ultra-low-noise microwave synthesis, broadband spectroscopy applications, and stable long-term calibration of astronomical spectrographs for exoplanet detection[5]. Further development of the technology beyond the first stabilization of the Ti:sapphire laser that heralded the frequency comb's arrival has enabled frequency combs to reach applications across many wavelength bands. The technology is reaching maturity, and frequency combs have been commercially available for some time.

In the last decade, methods for generating optical frequency combs without a mode-locked laser have suggested the possibility of bringing their capabilities to a wide set of applications outside the controlled environment of the research laboratory. These new frequency combs come with higher repetition rates, which makes them particularly attractive for applications where high power per comb mode, individual accessibility of comb modes, and fast acquisition times are desired; these applications include arbitrary microwave and optical waveform generation, telecommunications, and broadband, fast-acquisition-time spectroscopy. Moreover, these combs come with lower size, weight, and power (SWAP) requirements, which will enable them to bring the features that make mode-locked laser-based combs attractive into the field, enabling e.g. direct optical frequency synthesis on a chip [6].

This thesis focuses on this second generation of optical frequency combs. The bulk of the thesis covers microresonator-based frequency combs, and especially the nonlinear dynamics involved in the generation of these frequency combs via the Kerr nonlinearity. The penultimate chapter presents a second method for generating a high-repetition-rate frequency comb without modelocking that is based on active modulation of a seed CW laser and subsequent nonlinear spectral broadening. In the final chapter, I present experimental and theoretical investigations of a technique for repetition-rate reduction of frequency combs, which may prove useful for adapting low-SWAP combs and their intrinsically high repetition rates to some applications as the technology continues to develop.

In the remainder of this chapter, I discuss the basic properties of frequency combs and explain how the optical frequencies making up a comb can be fully determined by electronics operating with gigahertz-scale bandwidths.

1.1 Optical frequency combs

An optical frequency comb is obtained by fully stabilizing the spectrum of an optical pulse train. The first frequency combs came about through full frequency-stabilization of modelocked lasers; this thesis focuses on frequency combs with pulse trains generated through other means.

1.1.1 Optical pulse trains and their spectra

In the time domain, a frequency comb consists of a train of uniformly spaced optical pulses arriving at the pulse train's repetition rate f_r. These pulses are typically very short compared to their repetition period $T = 1/f_r$. In the frequency domain, the comb consists of a set of modes that are spaced by f_r in frequency and that have amplitudes determined by an overall spectral envelope centered at the optical carrier frequency, with bandwidth inversely related to the temporal duration of the pulses. The usual description of a frequency comb, which is natural for modelocked-laser-based combs that are not derived from a CW laser, gives the frequencies of these modes as

$$\nu_n = nf_r + f_0, \tag{1.1}$$

where $n \sim f_{carrier}/f_r$ for the optical modes that make up the comb and f_0 is the carrier-envelope offset frequency, which may be defined to be between 0 and f_r. The offset frequency results from the pulse-to-pulse evolution of the carrier wave underneath the temporal intensity envelope of the pulses due to a difference in group and phase velocities. An equivalent representation of the frequencies of the comb that is more natural for frequency combs directly derived from a CW laser, as described in this thesis, is

$$\nu_\mu = \nu_c + \mu f_r, \tag{1.2}$$

where ν_c is the frequency of the CW laser, the 'pump' or 'seed' laser, from which the frequency comb is derived and μ is a pump-referenced mode number, in contrast with the zero-referenced mode number n of Eq. 1.1. Fig. **??** depicts the properties of a frequency comb in the time domain and the frequency domain.

It is useful to consider a mathematical treatment of an optical pulse train to understand the relationships presented above. In the time domain, the electric field $E(t)$ of the pulse train consists of optical pulses that arrive periodically and have baseband (centered at zero frequency) field envelope $A(t)$ multiplying the carrier wave of angular frequency ω_c:

$$E(t) = \sum_{k=-\infty}^{\infty} A(t - kT)e^{i\omega_c t}. \tag{1.3}$$

Here, T is the repetition period of the pulse train. Eq. 1.3 can be viewed as describing a laser of angular frequency ω_c with a time-varying amplitude. This temporal modulation leads to the distribution of the power across a spectrum whose width scales inversely with the temporal duration of A. Intuitively, the spectrum of the comb is the spectrum of the periodic baseband field envelope $\Sigma_k A(t-kT)$, shifted by the multiplication with $e^{i\omega_c t}$ so that it is centered around the optical carrier.

More formally, we can calculate the spectrum $|\mathcal{F}\{E\}|^2$ by calculating

$$\mathcal{F}\{E\}(\omega) \sim \left(\sum_{k=-\infty}^{\infty} \mathcal{F}\{A(t-kT)\} \right) * \delta(\omega - \omega_c), \tag{1.4}$$

which results from the convolution (denoted by $*$) theorem for Fourier transforms. We use the Fourier transform's property that a temporal translation results in a linear spectral phase shift to obtain:

$$\mathcal{F}\{E\} \sim \left(\mathcal{F}\{A\} \times \sum_{k=-\infty}^{\infty} e^{-i\omega kT} \right) * \delta(\omega - \omega_c). \tag{1.5}$$

The quantity $\Sigma_k e^{-i\omega kT}$ is the Fourier-series representation of the series of δ-functions $\Sigma_\mu \delta(\omega - 2\pi\mu/T)$, so we get

$$\mathcal{F}\{E\}(\omega) \sim \left(\mathcal{F}\{A\} \times \sum_{\mu=-\infty}^{\infty} \delta\left(\omega - 2\pi\mu/T\right) \right) * \delta(\omega - \omega_c), \tag{1.6}$$

and performing the convolution leads to the replacement of ω with $\omega - \omega_c$, leading to:

$$\mathcal{F}\{E\} \sim \sum_{\mu=-\infty}^{\infty} \delta\left(\omega - \omega_c - \mu\omega_r\right) \mathcal{F}\{A\}(\omega - \omega_c). \tag{1.7}$$

This expression indicates that the spectrum of the comb has frequency content at modes $\nu_\mu = \nu_c + \mu f_r$, and that their amplitudes are determined by the spectrum of the baseband field envelope, shifted up to the optical carrier frequency ν_c. This is the natural formulation in the case of a comb derived from a CW laser, but it obscures the carrier-envelope offset frequency in the difference between ν_c and the nearest multiple of the repetition rate, so that f_0 is the remainder of $\nu_c \div f_r$. In practice, if f_r is known, then a measurement of f_0 is equivalent to a measurement of the frequency of the input CW laser.

1.1.2 Frequency stabilization of optical pulse trains

The scientific need for a method to measure optical frequencies motivated the development of optical frequency combs. While the measurement bandwidth of electronic frequency counters has improved since 1999, it remains limited to frequencies roughly one *million* times lower than the frequency of, e.g., visible red light. Frequency combs present a method for measurement of the unknown frequency f_{opt} of an optical signal through heterodyne with a frequency comb—if f_{opt}

falls within the bandwidth of the frequency comb, then the frequency of the heterodyne between the comb and the signal is guaranteed to be less than $f_r/2$, which is typically a frequency that can be measured electronically, at least for modelocked-laser-based combs. Therefore, if the frequencies of the comb are known, measurement of the heterodyne of the comb with the signal reveals the frequency of the signal, provided that the comb mode number n, as defined by Eq. 1.1, can be determined. This can be done via a wavelength measurement if sufficient precision is available, or by measuring the change $\partial f_b/\partial f_r = \pm n$, where f_b is the measured frequency of the beat.

The unique utility of the optical frequency comb lies in the fact that measurement of the two frequencies f_r and f_0, along with a measurement of the spectral envelope, is sufficient to determine the optical frequencies of all of the modes of the comb, thereby enabling frequency measurement of optical signals. Measurement of the repetition rates of optical pulse trains was possible for many years before the realization of optical frequency comb technology, as this can be done by simply impinging the pulse train on a photodetector. It was the confluence of several technological developments around the turn of the twenty-first century that allowed detection and measurement of the carrier-envelope offset frequency , thereby enabling creation of fully-stabilized modelocked-laser cite pulse trains: optical frequency combs.

The carrier-envelope offset frequency of a pulse train is challenging to measure because it describes evolution of the optical carrier wave underneath the intensity envelope, and therefore cannot be measured through straightforward detection of the intensity of the pulse train. Presently, the most straightforward way to measure f_0 is $f-2f$ *self-referencing*, which is illustrated in Fig.**??**. make fig This can be performed only with a pulse train whose spectrum spans an octave—a factor of two in frequency. Given such an octave-spanning supercontinuum spectrum, a group of modes near mode number N is frequency-doubled in a medium with the $\chi^{(2)}$nonlinearity[7]. This frequency-doubled light is heterodyned with the native light in the supercontinuum with mode number near $2N$. The frequency of the resulting beat f_b is:

$$f_b = f_{doubled} - f_{native} \tag{1.8}$$

$$= 2(Nf_r + f_0) - (2Nf_r + f_0) \tag{1.9}$$

$$= f_0. \tag{1.10}$$

Generating the necessary octave-spanning supercontinuum spectrum typically requires nonlinear spectral broadening of the pulse train after its initial generation, except for in specific, carefully engineered cases. Achieving the required degree of spectral broadening while preserving the coherence properties of the pulse train is a significant challenge—typically this requires launching a train of high energy (∼1 nJ), temporally short (≤ 100 fs) pulses into the spectral-broadening stage, and meeting these requirements is one of the important engineering considerations in designing optical frequency comb systems, as discussed in Chapters **??** and **??**.

cite Tara, others

Chapter 2

Introduction to microresonator-based frequency combs

This chapter introduces the basic physics of optical frequency-comb generation in Kerr-nonlinear microresonators, with an emphasis on providing context for the results described in the subsequent chapters. A number of papers that review the topic have been published, each of which provides a unique perspective on this rapidly evolving field [**Kippenberg2011**, **Savchenkov2016**, **Chembo2017**, **Pasquazi2018**].

look at: frequency combs: cavity solitons come of age

For simplicity, we will refer to broadband optical spectra generated through frequency conversion in Kerr-nonlinear resonators as 'Kerr combs,' even when the output is not strictly a frequency comb. So far researchers have focused on Kerr-comb generation using microresonators with a ring geometry—so-called microring resonators. It is also possible to generate Kerr combs in a Kerr-nonlinear Fabry-Perot (FP) cavity, as has been recently demonstrated by Obrzud, Lecomte, and Herr [8]. Theoretical investigations of Kerr-comb generation with the FP geometry are presented in Chapter **??**.

2.1 Optical microring resonators

An optical microring resonator, shown schematically in Fig. **??**, guides light around a closed path in a dielectric medium by total internal reflection. The principle is the same as the guiding of light in an optical fiber, and indeed a 'macroring' resonator can be constructed from a loop of fiber, using a fiber-optic coupler with a small coupling ratio as an input/output port. Ring resonators are sometimes referred to as whispering-gallery mode resonators due to the similarity between their guided modes and the acoustic 'whispering-gallery' waves that permit a listener on one side of St. Paul's cathedral to hear whispers uttered by a speaker on the other side of the cathedral, as explained by Lord Rayleigh beginning in 1910. Optical microring resonators have a host of characteristics that make them useful for nonlinear optics and photonics applications; these include the ease with which they can be integrated, the ultra-high quality (Q) factors that have been demonstrated, and the ability to tailor the spectral distribution of guided modes through careful resonator design.

A microring resonator supports propagating guided optical modes of electromagnetic radiation with (vacuum) wavelengths that evenly divide the optical round-trip path length: $\lambda_m = n_{eff}(\lambda_m)L/m$, with associated resonance frequencies $\nu_m = c/\lambda_m = mc/n_{eff}(\nu_m)L$. This leads to constructive interference from round-trip to round-trip. Here L is the physical circumference of the resonator, m is the azimuthal mode number, and $n_{eff}(\lambda_m)$ is an effective index of refraction that depends on the resonator geometry and the transverse intensity profile of the mode (see e.g. [**REFHERE**] for more information). The free-spectral range f_{FSR} of a resonator is the *local* frequency spacing between modes, calculated via:

$$\begin{aligned} f_{FSR} &\approx \nu_{m+1} - \nu_m \approx \nu_m - \nu_{m-1}, && (2.1)\\ &= \frac{\partial \nu_m}{\partial m}, && (2.2)\\ &= \frac{c}{n_{eff}(\nu)L} - \frac{mc}{n_{eff}^2(\nu)L}\frac{\partial n_{eff}}{\partial \nu}\frac{\partial \nu}{\partial m}, && (2.3)\\ \Rightarrow f_{FSR} &= \frac{c/L}{\left(n_{eff} + \nu\frac{\partial n_{eff}}{\partial \nu}\right)} = \frac{c}{n_g L} = 1/T_{RT}, && (2.4) \end{aligned}$$

where $n_g = n_{eff} + \nu\frac{\partial n_{eff}}{\partial \nu}$ is the group velocity of the mode and T_{RT} is the mode's round-trip time. The effective index n_{eff} is frequency dependent due to both intrinsic material dispersion and geometric dispersion, where the latter results for example from different sampling of core versus cladding material properties for different wavelength-dependent mode areas. A frequency-dependent n_{eff} leads to a frequency dependence of n_g and f_{FSR}, and a resulting non-uniform spacing in the cavity modes in frequency despite the linearity of ν_m in m.

Depending on the design, microring resonators can support a single propagating transverse mode profile or may be multi-mode, meaning that many different transverse mode profiles are supported. The former can be readily achieved using chip-integrated photonic waveguides that provide index contrast and transverse confinement on four sides; the latter is typical of resonators that lack an inner radius dimension and therefore exhibit less spatial confinement, such as free-standing silica microrod resonators [9]. For a given resonator geometry, to calculate the frequency-dependent effective index $n_{eff}(\nu)$, thereby enabling calculation of the resonance frequencies and wavelengths, one must solve Maxwell's equations for the resonator geometry. Except in special cases of high symmetry [10], this is typically done numerically using finite-element modeling tools like COMSOL. The modes of an optical resonator, both within a mode family defined by a transverse mode profile and between mode families, must be orthogonal[11], meaning that there is no linear coupling between them.

2.1.1 Resonant enhancement in a microring resonator

The lifetime τ_γ of circulating photons in a resonator is fundamental to its fitness for applications. Generally, two processes lead to the loss of circulating photons: intrinsic dissipation that occurs at a rate $1/\tau_{int}$ and outcoupling to an external waveguide that occurs at a rate $1/\tau_{ext}$, leading to a total loss rate of $\tau_\gamma^{-1} = \tau_{ext}^{-1} + \tau_{int}^{-1}$. To understand the quantitative role of these parameters, we consider a cavity mode of frequency ω_0 and amplitude a (normalized such that $|a|^2 = N$, the number of circulating photons) driven by a field with frequency Ω_0 and rotating amplitude $s \propto \exp(i\Omega_0 t)$ (normalized such that $|s|^2 = S$, the rate at which photons in the coupling waveguide pass the coupling port) that is in-coupled with strength κ. The equation of motion for such a system is[11]:

$$\frac{da}{dt} = i\omega_0 a - \left(\frac{1}{2\tau_{int}} + \frac{1}{2\tau_{ext}}\right) a + \kappa s. \tag{2.5}$$

We can immediately solve this equation by assuming that $a \propto \exp(i\Omega_0 t)$, and we obtain:

check this and all the math here

$$a = \frac{\kappa s}{\left(\frac{1}{2\tau_{int}} + \frac{1}{2\tau_{ext}}\right) + i(\Omega_0 - \omega_0)}. \tag{2.6}$$

To extract anything further from this equation, we must derive a relationship between τ_{ext} and κ, which so far are not related. To do this, we exploit the time-reversal symmetry that is inherent in this system when there is no dissipation, that is, when $1/\tau_{int} = 0$. In the case of only an initial excitation N_0 decaying into the waveguide with the driving term s set to zero, we have $N = N_0 e^{-t/\tau_{ext}}$. In this case, energy conservation guarantees that the rate S_{out} at which photons propagate away from the resonator in the waveguide is $S_{out} = -dN/dt = N_0 e^{-t/\tau_{ext}}/\tau_{ext}$; we therefore have $S_{out} = N/\tau_{ext}$. In the time-reversed system with $t \to -t$, this amplitude S_{out} describes the rate of pumping: the cavity is resonantly driven with increasing power $S = S_{out}(-t) = N_0 e^{t/\tau_{ext}}/\tau_{ext}$. In this case the frequency of the driving field s can be written $\omega_0 - i/2\tau_{ext}$. Inserting this frequency into Eq. 2.6 gives the equations

$$a = \kappa s \tau_{ext} \tag{2.7}$$

and

$$N = |\kappa|^2 S \tau_{ext}^2. \tag{2.8}$$

By comparing the relationships between S_{out} and N for the forward-evolving system and S and N for the backward-evolving system, we arrive at the relationship $|\kappa|^2 = 1/\tau_{ext}$. We can return to the case including dissipation and insert this expression for κ into Eq. 2.6, which can then be squared to obtain:

$$N = \frac{\Delta\omega_{ext} S}{\Delta\omega_{tot}^2/4 + (\Omega_0 - \omega_0)^2} \tag{2.9}$$

Here we define the linewidths $\Delta\omega_{ext} = 1/\tau_{ext}$, $\Delta\omega_{int} = 1/\tau_{int}$, and $\Delta\omega_{tot} = \Delta\omega_{ext} + \Delta\omega_{int}$. Two important observations can be drawn from Eq. 2.9: First, the cavity response is Lorentzian with a full-width at half-maximum (FWHM) linewidth that is related to the photon lifetime via $\tau_\gamma = 1/\Delta\omega_{tot}$, and second, on resonance the number of circulating photons is related to the input rate by the factor $\Delta\omega_{ext}/\Delta\omega_{tot}^2$. The combination of this resonant enhancement and a small cavity mode volume enables very large circulating optical intensities, which is important for the application of microresonators in nonlinear optics.

Two commonly used practical quantities are linked to the photon lifetime: the resonator finesse $\mathcal{F} = 2\pi\tau_\gamma/T_{RT}$, which for a ring resonator can be interpreted literally as the azimuthal resonator angle traced out by a typical photon over its lifetime; and the resonator quality factor $Q = \omega_c\tau_\gamma$, the phase over which the optical field evolves during the photon lifetime. Using the relationship $\tau_\gamma = 1/\Delta\omega_{tot}$, the finesse and quality factor can be rewritten as simple ratios of the relevant frequencies: $\mathcal{F} = f_{FSR}/\Delta\nu$; $Q = \nu_c/\Delta\nu$, where $\Delta\nu = \Delta\omega_{tot}/2\pi$.

2.1.2 Thermal effects in microresonators

In a typical microresonator frequency-comb experiment, a frequency-tunable pump laser is coupled evanescently into and out of the resonator using a tapered optical fiber[12] (for e.g. free-standing silica disc resonators) or a bus waveguide (for chip-integrated resonators, e.g. in silicon nitride rings). When spatial overlap between the evanescent mode of the fiber and a whispering-gallery mode of the resonator is achieved, with the frequency of the pump laser close to the resonant frequency of that mode, light will build up in the resonator and the transmission of the pump laser past the resonator will decrease.

In any experiment in which a significant amount of pump light is coupled into a resonator, one immediately observes that the cavity resonance lineshape in a scan of the pump-laser frequency is not Lorentzian as expected from Eq. 2.9. This is due to heating of the resonator as it absorbs circulating optical power. Since the volume of a pumped mode and the physical volume of the microresonator are both small, thermal effects have significant practical implications in microresonator experiments. As the volume of the mode heats (over a 'fast thermal timescale') and this energy is conducted to and heats the rest of the resonator (over the 'slow thermal timescale') [13], the resonance frequency of a given cavity mode shifts due to the thermo-optic coefficient $\partial n/\partial T$ and the coefficient of thermal expansion of the mode volume $\partial V/\partial T$. For typical microresonator materials the thermo-optic effect dominates, and $\partial n/\partial T > 0$ leads to a decrease in the resonance frequency with increased circulating power in steady state.

A calculation of the thermal dynamics of the system [14] composed of the pump laser and the resonator reveals that there is a range of pump-laser frequencies Ω_0 (that depends on the pump laser power) near and below the 'cold-cavity' resonance frequency of a given cavity mode over which the system has three possible thermally-shifted resonance frequencies $\omega_{0,shifted}$ at which thermal steady state is achieved. Generally, these points are:

(1) $\Omega_o > \omega_{0,shifted}$, blue detuning with significant coupled power and thermal shift

(2) $\Omega_o < \omega_{0,shifted}$, red detuning with significant coupled power and thermal shift

(3) $\Omega_o \ll \omega_{0,shifted}$, red detuning with insignificant coupled power and no thermal shift

Steady-state point (1) is experimentally important, because in the presence of pump-laser frequency and power fluctuations it leads to so-called thermal 'self-locking.' Specifically for steady-state point (1), this can be seen as follows:

- If the pump-laser power increases the cavity heats, the resonance frequency decreases, the detuning increases, and the change in coupled power is minimized.
- If the pump-laser power decreases the cavity cools, the resonance frequency increases, the detuning decreases, and the change in coupled power is minimized.
- If the pump-laser frequency increases the cavity cools, the resonance frequency increases, and the change in coupled power is minimized.
- If the pump-laesr frequency decreases the cavity heats, the resonance frequency decreases, and the change in coupled power is minimized.

This is in contrast with steady-state point (2), where each of the four pump-laser fluctuations considered above generates a positive feedback loop, with the result that any fluctuation will push the system towards point (1) or point (3). This preference of the system to occupy point (1) or point (3) over a range of pump-laser detuning is referred to as thermal bistability. One consequence of this bistability is that the transmission profile of the pump laser takes on hysteretic behavior in a scan over a cavity resonance with significant pump power: in a decreasing frequency scan, the lineshape takes on a broad sawtooth shape, while in an increasing frequency scan, the resonance takes on a narrow pseudo-Lorentzian profile whose exact shape depends on the scan parameters relative to the thermal timescale. This is shown in Fig. **??**. A second consequence is that operation at red detuning with significant coupled power in a microresonator experiment requires special efforts to mitigate the effects of thermal instability.

2.2 Microring resonator Kerr frequency combs

The high circulating optical intensities accessible in resonators with long photon lifetimes find immediate application in the use of microresonators for nonlinear optics. The experiments described in this thesis are conducted in silica microresonators. Silica falls into a broader class of materials that exhibit both centro-symmetry, which dictates that the second-order nonlinear susceptibility $\chi^{(2)}$ must vanish, and a significant third-order susceptibility $\chi^{(3)}$. The n^{th}-order susceptibility is a term in the Taylor expansion describing the response of the medium's polarization to an external electric field[7]: $P = P_0 + \epsilon_0\chi^{(1)}E + \epsilon_0\chi^{(2)}E^2 + \epsilon_0\chi^{(3)}E^3 + ...$ The effect of $\chi^{(3)}$ can be described in a straightforward way as a dependence of the refractive index on the local intensity[15],

$$n = n_0 + n_2 I \tag{2.10}$$

where $n_2 = \frac{3\chi^{(3)}}{4n_0^2\epsilon_0 c}$[15, 16]. The intensity-dependence of the refractive index resulting from the third-order susceptibility $\chi^{(3)}$ is referred to as the optical Kerr effect.

The combination of the Kerr effect and the high circulating intensities that are accessible in high-finesse cavities provides a powerful platform for nonlinear optics. Specifically, the Kerr effect enables self-phase modulation, cross-phase modulation, and four-wave mixing, the last of which is depicted schematically in Fig. **??**.

In 2007, a remarkable result brought the beginning of a new era for frequency comb research. Del'Haye et al reported *cascaded four-wave mixing* (CFWM) in toroidal silica microcavities on silicon chips, the result of which was a set of many co-circulating optical fields that were uniformly spaced by f_{rep} ranging from 375 GHz to ∼750 GHz (depending on the platform)[17]. Measurements indicated that the frequency spacing was uniform to a precision of 7.3×10^{-18}, thereby establishing that the output of the system was a frequency comb. This result built on previous demonstrations of few-mode parametric oscillations in microresonators [18–20], and showed that the non-uniform distribution of cavity resonance frequencies due to dispersion could be overcome to generate an output with equidistant frequency modes. A second important development occurred in 2012, when Herr et al. reported the generation of frequency combs corresponding in the time domain to single circulating optical 'soliton' pulses. This observation followed the observation of solitons in formally-equivalent passive fiber-ring resonators in 2010[21]. Due to unique properties that make them particularly well-suited for applications, as discussed in Sec. 2.6, the generation and manipulation of soliton combs has become a significant priority in microcomb research.

2.3 A model for Kerr-comb nonlinear optics: The Lugiato-Lefever equation

Kerr-comb generation can be motivated and partially understood through the CFWM picture [22], but the phase and amplitude degrees of freedom for each comb line mean that CFWM gives rise to a rich space of comb phenomena—it is now known that Kerr combs can exhibit several fundamentally distinct outputs. A useful model for understanding this rich space is the Lugiato-Lefever equation (LLE), which was shown to describe microcomb dynamics by Chembo and Menyuk [23] through Fourier-transformation of a set of coupled-mode equations describing CFWM and by Coen, Randle, Sylvestre, and Erkintalo [24] through time-averaging of an Ikeda map for a low-loss resonator (as first performed by Haelterman, Trillo, and Wabnitz [25]). The LLE is a nonlinear partial-differential equation that describes evolution of the normalized cavity field envelope ψ over a slow time $\tau = t/2\tau_\gamma$ in a frame parametrized by the ring's azimuthal angle θ (running from $-\pi$ to π) co-moving at the group velocity. The equation as formulated by Chembo and Menyuk, as it will be used throughout this thesis, reads:

$$\frac{\partial \psi}{\partial \tau} = -(1 + i\alpha)\psi + i|\psi|^2\psi - i\frac{\beta}{2}\frac{\partial^2 \psi}{\partial \theta^2} + F. \tag{2.11}$$

This equation describes ψ over the domain $-\pi \leq \theta \leq +\pi$ with periodic boundary conditions $\psi(-\pi, \tau) = \psi(\pi, \tau)$. Here F is the normalized strength of the pump laser, with F and ψ both normalized so that they take the value 1 at the absolute threshold for cascaded four-wave mixing:

$F = \sqrt{\frac{8g_0\Delta\omega_{ext}}{\Delta\omega_{tot}^3}\frac{P_{in}}{\hbar\Omega_0}}$, $|\psi|^2 = \frac{2g_0 T_{RT}}{\hbar\omega\Delta\omega_{tot}}P_{circ}(\theta,\tau)$, so that $|\psi(\theta,\tau)|^2$ is the instantaneous normalized power at the co-moving azimuthal angle θ. Here $g_0 = n_2 c\hbar\Omega_0^2/n_g^2 V_0$ is a parameter describing the four-wave mixing gain, $\Delta\omega_{ext}$ is the rate of coupling at the input/output port, $\Delta\omega_{tot} = 1/\tau_\gamma$ is the FWHM resonance linewidth, P_{in} is the pump-laser power, P_{circ} is the circulating power in the cavity, $\hbar$ is Planck's constant, and Ω_0 is the pump-laser frequency. The parameters n_2, n_g, and V_0 describe the nonlinear (Kerr) index (see Eqn. 2.10), the group index of the mode, and the effective nonlinear mode volume at the pump frequency; L is the physical round-trip length of the ring cavity.

The parameters α and β describe the normalized frequency detuning of the pump laser and second-order dispersion of the resonator mode family into which the pump laser is coupled: $\alpha = -\frac{2(\Omega_0-\omega_0)}{\Delta\omega_{tot}}$, $\beta = -\frac{2D_2}{\Delta\omega_{tot}}$; here $D_2 = \left.\frac{\partial^2\omega_\mu}{\partial\mu^2}\right|_{\mu=0}$ is the second-order modal dispersion parameter, where μ is the pump-referenced mode number of Eq. 1.2. The parameters $D_1 = \left.\frac{\partial\omega_\mu}{\partial\mu}\right|_{\mu=0} = 2\pi f_{FSR}$ and D_2 are related to the derivatives of the propagation constant $\beta_{prop} = n_{eff}(\omega)\omega/c$ via $D_1 = 2\pi/L\beta_1$ and $D_2 = -\frac{D_1^2}{\beta_{prop,1}}\beta_{prop,2}$, where $\beta_{prop,n} = \partial^n\beta_{prop}/\partial\omega^n$. The subscript *prop* is used here to distinguish the propagation constant from the LLE dispersion coefficients $\beta_n = -2D_n/\Delta\omega_{tot}$, as unfortunately the use of the symbol β for both of these quantities is standard. Expressions for higher-order modal dispersion parameters D_n in terms of the expansion of the propagation constant can be obtained by evaluating the equation $D_n = (D_1\frac{\partial}{\partial\mu})^n\omega_\mu$. check

The formulation of the LLE in terms of dimensionless normalized parameters helps to elucidate the fundamental properties of the system and facilitates comparison of results obtained in platforms with widely different experimental conditions. In words, the LLE relates the time-evolution of the intracavity field (normalized to its threshold value for cascaded four-wave mixing) to the power of the pump laser (normalized to its value at the threshold for cascaded four-wave mixing), the pump-laser detuning (normalized to half the cavity linewidth), and the cavity second-order disperison quantified by the change in the FSR per mode (normalized to half the cavity linewidth). One example of the utility of this formulation is that it makes apparent the significance of the cavity linewidth in determining the output comb, and underscores the fact that optimization of the dispersion, for example, without paying heed to the effect of this optimization on the cavity linewidth, may not yield the desired results.

The LLE is, of course, a simplified description of the dynamics occurring in the microresonator. It abstracts the nonlinear dynamics and generally successfully describes the various outputs that can be generated in a microresonator frequency comb experiment. The LLE is a good description of these nonlinear dynamics when the resonator photon lifetime, mode overlap, and nonlinear index n_2 are roughly constant over the bandwidth of the generated comb, and when the dominant contribution to nonlinear dynamics is simply the self-phase modulation term $i|\psi|^2\psi$ arising from the Kerr nonlinearity. The LLE neglects polarization effects, thermal effects, and the Raman scattering and self-steepening nonlinearities, although in principle each of these can be included [15, 26–28]. It is also worth emphasizing that the LLE can be derived from a more formally-accurate Ikeda map (as is done by Coen et al. [24]), in which the effect of localized input- and output-coupling is included in the model. This is achieved by 'delocalizing' the pump field and the output-coupling over the round trip, including only their averaged effects. This is an approximation that is valid in the limit of high finesse due to the fact that the cavity field cannot change on the timescale of a single round trip, but as a result the LLE necessarily neglects all dynamics that might have some periodicity at the round-trip time; the fundamental timescale of LLE dynamics is the photon lifetime.

The LLE provides a useful framework for the prediction and interpretation of experimental results. Basically, it predicts the existence of two fundamentally distinct types of Kerr-combs: extended temporal patterns and localized soliton pulses. These predictions are born out by experiments, the interpretation of which is facilitated by insight gained from the LLE. In the remainder of this chapter I briefly present some simple analytical results that can be obtained from the LLE, and then discuss these two types of comb outputs. This discussion provides context for the results presented in the next two chapters. Fig. **??** summarizes the results that will be presented in the remainder of this chapter.

2.4 Analytical investigation of the resonator's CW response

Some insight into comb dynamics can be obtained via analytical investigations of the LLE, Eq. 2.11. This section largely follows the analysis of Ref. [29], with similar analysis having been performed elsewhere, for example in Refs. [24] and [30]. When the derivative term $\partial^2\psi/\partial\theta^2$ inthe LLE is non-zero, ψ is necessarily broadband, and a Kerr comb has been formed. There are no known exact analytical solutions to the LLE to describe Kerr-comb outputs. However, flat solutions to the LLE ψ_s may be calculated by setting all derivatives to zero—when these solutions can be realized physically (discussed below), they describe the behavior of the CW field that exists in the resonator in the absence of Kerr-comb formation. Upon setting the derivatives to zero, one finds:

$$F = (1 + i\alpha)\psi_s - i|\psi_s|^2\psi_s. \tag{2.12}$$

The circulating intensity $\rho = |\psi_s|^2$ is obtained by taking the modulus-square of Eq. 2.12 to get:

$$F^2 = \left(1 + (\alpha - \rho)^2\right)\rho, \tag{2.13}$$

whereupon this equation can be solved for ρ. With α held constant, the function $F^2_\alpha(\rho)$ defined by this equation uniquely determines F^2 for a given value of ρ. By noting that $F^2(\rho = 0) = 0$ and $\partial F^2/\partial\rho\big|_{\rho=0} > 0$, one can conclude that three real solutions for the inverted function $\rho_\alpha(F^2)$ exist between the values $\rho_\pm$ that extremize $F^2_\alpha(\rho)$:

$$\rho_\pm = \frac{2\alpha \pm \sqrt{\alpha^2 - 3}}{3}, \tag{2.14}$$

while outside of this interval there is only one real solution $\rho_\alpha(F^2)$ exists.

Physically, the coexistence of multiple flat solutions ρ at a given point (α, F^2) corresponds to a 'tilting' of the Lorentzian transmission profile of the cavity and leads to bistability, even before taking into account thermal effects. This is illustrated in Fig. **??**. Generally speaking, extended patterns exist on the upper branch of this curve, highlighted in blue, and solitons exist on the lower branch, highlighted in red. For flat solutions ρ, an effective Kerr-shifted detuning can be defined as $\alpha_{eff} = \alpha - \rho$. The discussion of thermal effects in Sec. 2.1.2 then applies to the effective detuning

α_{eff}; that is, operating with significant coupled power at *effective* red-detuning is thermally unstable, while thermal locking occurs with significant coupled power at effective blue detuning. The effective detuning simply incorporates the Kerr nonlinearity into the round-trip phase shift that describes the constructive or destructive interference of the circulating field with the pump at the coupling port. By noting that $\alpha = F^2 = \rho$ solves Eq. 2.13, we can conclude that the position of the effective Kerr-shifted resonance is on the line $\alpha = F^2$, where $\alpha_{eff} = 0$. For fixed F^2, an effectively red-detuned branch of the tilted resonance exists above the value of α where ρ becomes multivalued. This value of α can be determined by inserting ρ_- (Eq. 2.14) into Eq. 2.13 and solving for α.

Once the circulating intensity ρ is known, the corresponding flat solution ψ_s can be determined from Eq. 2.12 by inserting the known value of ρ and solving for ψ_s, with the result:

$$\psi_s = \frac{F}{1 + i(\alpha - \rho)}. \tag{2.15}$$

This expression reveals that the flat solution acquires a phase $\phi_{CW} = \tan^{-1}(\rho - \alpha)$ relative to the pump.

If the flat solution(s) at a point (α, F^2) is (are) unstable, a Kerr comb will form spontaneously. Stability analysis of the flat solutions can be performed, and the results are [29]:

- In the region of multi-stability, if the flat solutions are ordered with increasing magnitude as ρ_1, ρ_2, and ρ_3, the middle solution ρ_2 is always unstable.

- A flat solution ρ that is not the middle solution is stable if $\rho < 1$; otherwise it is unstable. When the flat solution is unstable, the mode that experiences the greatest instability has mode number $\mu_{max} = \sqrt{\frac{2}{\beta}(\alpha - 2\rho)}$.

Therefore, the pump-laser threshold curve for Kerr-comb generation can be determined in the $\alpha - F^2$ plane by setting $\rho = 1$ in Eq. 2.12:

$$F^2_{thresh} = 1 + (\alpha - 1)^2, \tag{2.16}$$

$$\alpha_{thresh} = 1 \pm \sqrt{F^2 - 1}, \tag{2.17}$$

for an experiment in which the pump power or detuning is tuned while the other is held fixed.

2.5 Kerr comb outputs: extended modulation-instability patterns

Extended temporal patterns arise spontaneously as a result of the instability of the flat solution to the LLE when the pump laser is tuned above the threshold curve. These patterns can be stationary, in which case they are typically referred to as 'Turing patterns' or 'primary comb,' or can evolve in time, in which case they are typically referred to as 'noisy comb' or 'spatiotemporal chaos.' In general, the former occurs for lower values of the detuning α and smaller pump strengths F^2; although some studies of the transition from Turing patterns to chaos have been conducted [**others**, 31], a well-defined boundary between the two has not been established, and may not exist.

In the spatial domain parametrized by θ, a Turing pattern consists of a pulse train with (typically) $n \gg 1$ pulses in the domain $-\pi \leq \theta \leq \pi$—the pulse train's repetition rate is a multiple of the cavity FSR: $f_{rep} = n \times f_{FSR}$. Corresponding to the n-fold decreased period (relative to the round-trip time) of an n-pulse Turing pattern's modulated waveform in the time domain, the optical spectrum of a Turing pattern consists of modes spaced by n resonator FSR—it is this widely-spaced spectrum that is referred to as 'primary comb.' Analytical approximations for Turing patterns are possible near threshold [32, 33] and in the small damping limit [34]. The stability analysis results from the last section can be used to predict the spacing n of a primary comb (equivalently the number of Turing-pattern pulses) generated in a decreasing-frequency scan across the resonance with fixed normalized pump power F^2: $n = \mu_{max,thresh} = \sqrt{\Delta\omega_0(1 + \sqrt{F^2 - 1})/D_2}$.

Spatiotemporal chaos can be understood as a Turing pattern whose pulses oscillate in height, with adjacent pulses oscillating out of phase. From such an oscillating Turing pattern, if α and/or F^2 is increased, one moves deeper into the chaotic regime and pulses begin to exhibit lateral motion and collisions; the number of pulses present in the cavity is no longer constant in time. Depending on the severity of the chaos (higher for larger α and F^2), a chaotic comb may correspond to a primary-comb-type spectrum with each primary-comb mode exhibiting sidebands at the resonator FSR, so-called 'subcombs,' or it may correspond to a densely-populated spectrum with light in each cavity mode.

Relative to generation of solitons, experimental generation of an extended pattern is straightforward. As shown in Fig. ??, these patterns are generated with blue effective pump-laser detuning $\alpha_{eff} < 0$, where thermal locking occurs. Because they arise spontaneously from noise, their generation is (comparatively) straightforward: simply decrease the pump-laser frequency until a pattern is generated. Unfortunately, operation of a Kerr-comb in the extended pattern regime is disadvantageous for applications: the n-FSR spacing of primary comb presents a challenge for measurement of the repetition rate of the frequency comb due to the bandwidth of measurement electronics, and the aperiodic time-evolution of chaotic comb corresponds to modulation sidebands on the comb modes within the linewidth of the cavity that preclude the use of the comb as a set of stable optical reference frequencies.

An important property of these extended patterns is that they fill the resonator—the characteristic size of temporal features scales roughly as $1/\sqrt{-\beta}$, but these features are distributed densely and uniformly throughout the resonator. This means that the total circulating power of an extended pattern $\int d\theta\,|\psi|^2$ is large relative to the localized pulses discussed in the next section, and therefore that extended patterns come with a comparatively large thermal shift of the resonance.

2.6 Kerr comb outputs: solitons

The term 'soliton' generally refers to a localized excitation that can propagate without changing its shape due to a delicate balance between dispersion (or diffraction) and nonlinearity. Solitons are found in several contexts within the field of nonlinear optics, and temporal Kerr-soliton pulses in optical fibers are particularly well known. Microresonators support so-called dissipative cavity solitons, which are localized pulses circulating the resonator that are out-coupled once per round trip. In the case of a single circulating soliton, this leads to a train of pulses propagating away from the resonator with repetition rate $1/T_{RT}$. Thus the mode spacing of the comb matches the FSR of the resonator, in contrast with widely-spaced primary comb spectra, and the soliton can, in principle, propagate indefinitely as a stationary solution to the LLE. This makes Kerr combs based on solitons particularly attractive for applications.

Solitons in optical fibers are solutions of the nonlinear Schrodinger equation (NLSE) that describes pulse-propagation in optical fiber [15]:

$$\frac{\partial A}{\partial z} = i\gamma|A|^2 A - i\frac{\beta}{2}\frac{\partial^2 A}{\partial T^2}. \tag{2.18}$$

This equation describes the evolution of the pulse envelope A in the 'fast-time' reference frame parametrized by T as it propagates down the length of the fiber, parametrized by the distance variable z. Here γ is the nonlinear coefficient of the fiber and $\beta prop, 2$ is the GVD parameter. The LLE can be viewed as an NLSE with additional loss and detuning terms $-(1+i\alpha)\psi$ and a driving term F.

reference to the above, also do I need a 2 here

The fundamental soliton solution to the NLSE is:

$$A_{sol} = \sqrt{P_0}\,\mathrm{sech}\,(T/\tau)\; e^{i\gamma P_0 z/2 + i\phi_0}, \tag{2.19}$$

where P_0 is the peak power of the pulse and is related to the duration of the pulse τ via $\tau = \sqrt{-\beta/\gamma P_0}$, and ϕ_0 is an arbitrary phase. Thus, this equation admits a *continuum* of pulsed fundamental 'soliton' solutions, with one existing for each value of the peak power. Each of these solutions propagates down the fiber without changing shape; only the phase evolves with distance as $\phi(z) = \gamma P_0 z/2 + \phi_0$.

The introduction of the loss, detuning, and driving terms into the NLSE to obtain the LLE has several important consequences for solitons. First, exact analytical expressions for the soliton solution to the LLE in terms of elementary functions are not known, in contrast with the situation for the NLSE. However, the soliton solutions to the LLE, Eq. 2.11, can be approximated well as:

$$\psi_{sol} = \psi_{s,min} + e^{i\phi_0}\sqrt{2\alpha}\,\mathrm{sech}\sqrt{\frac{2\alpha}{-\beta}}\theta. \tag{2.20}$$

Here $\psi_{s,min}$ is the flat solution to the LLE from Eq. 2.15 at the point where the soliton solution is desired; when multiple flat solutions exist, $\psi_{s,min}$ is the one corresponding to the smallest intensity ρ_1. The phase $\phi_0 = \cos^{-1}(\sqrt{8\alpha}/\pi F)$ arises from the intensity-dependent phase shift in the cavity due to the Kerr effect, mathematically described by the term $i|\psi|^2\psi$.

This approximation ψ_{sol} from Eq. 2.20 for the soliton solution of the LLE illustrates a second important consequence of the differences between the NLSE and the LLE: while the NLSE admits a continuum of fundamental soliton solutions parametrized by their peak power P_0 and arbitrary phase ϕ_0, the LLE supports only one shape for the envelope of a soliton for fixed experimental parameters α and F^2. Intuitively, this can be understood as arising from the need for a balance between dispersion and nonlinearity, as in the NLSE, *and* between loss (described by $\partial\psi/\partial\tau = -\psi + ...$) and the pump (described by $\partial\psi/\partial\tau = ... + F$) for stable evolution of an LLE soliton—the driving term is not scaled by ψ, which instead would represent linear gain, and therefore provides an absolute reference that fixes the amplitude of the soliton.

The amplitude of the LLE soliton depends only on the detuning α, and the width of the soliton increases with larger detuning α and smaller dispersion β. These characteristics are apparent from the analytical approximation in Eq. **??**, but are also evident in numerical calculations of the exact soliton solution to the LLE[35].

check if this is an appropriate reference

Solitons exist only where there is a flat solution ψ_s that is effectively red detuned that can form the background for the pulse[30, 36]. Consistent with the phase ϕ_0 in the approximation ψ_{sol} in Eq. 2.20, solitons can exist up to a maximum detuning of $\alpha_{max} = \pi^2 F^2/8$ [27].

Solitons are strongly localized: the deviation of the background intensity from ρ_1 near a soliton at θ_0 is proportional to $e^{-(\theta-\theta_0)/\delta\theta}$, where $\delta\theta = \sqrt{-\beta/2\alpha}$. If $\delta\theta$ is sufficiently small, multiple solitons can be supported in the resonator domain $-\pi \leq \theta \leq \pi$ with negligible interactions between solitons. Simulations reveal that if $(\theta - \theta_0)/\delta\theta$ is too small, solitons exhibit attractive interactions; the result of this attraction can be pair-wise annihilation or pair-wise merger, with the ultimate result being a stable soliton ensemble with fewer solitons. The maximum number of solitons that can coexist in a resonator in the absence of higher-order stabilizing effects (see Chapter **??**) can be approximated as $N_{max} \approx \sqrt{-2/\beta}$ [27].

should I add some references here?

The spectrum of a single-soliton comb has a $\mathrm{sech}^2(\Omega_0/\Delta\Omega)$ envelope, where $\Delta\Omega \approx \sqrt{32\alpha/|\beta|T_{RT}^2}$ is the bandwidth of the pulse in angular frequency. Equivalently, the bandwidth of the soliton in (linear) optical frequency is $\sqrt{\frac{16\Delta\nu f_{rep}^2}{D_2}\alpha}$. For a soliton at the maximum detuning $\alpha_{max} = \pi^2 F^2/8$

for fixed normalized pump power F^2, the bandwidth is then $\sqrt{\frac{\pi^2 \Delta\nu f_{rep}^2}{2D_2}F^2}$. Because solitons have single-FSR spacing, have the output localized into a high peak-power pulse, and are stationary (in contrast with chaos, which has single-FSR spacing but is not-stationary), they are useful for applications. Many of the proposals for and demonstrations of applications with Kerr-combs have used single-soliton operation.

2.6.1 Experimental generation of solitons

Relative to the generation of extended modulation-instability patterns, experimental generation of solitons in microring resonators is challenging. Solitons are localized excitations below threshold, which means that their existence is degenerate with their absence—a resonator can host $N = 0, 1, 2, ...$ up to N_{max} solitons for a given set of parameters α and F^2; this degeneracy is illustrated in Fig. **??**. If α and F^2 are experimentally tuned to a point at which solitons may exist, ψ will evolve to a form determined by the initial conditions of the field ψ. To provide appropriate initial conditions, most experimental demonstrations of soliton generation have involved first generating an extended pattern in the resonator, and then tuning to an appropriate point (α, F^2) so that 'condensation' of solitons from the extended pattern occurs.

Condensation of solitons from an extended pattern presents additional challenges. First, it is difficult to control the number of solitons that emerge, due to the high degree of soliton-number degeneracy. This typically leads to a success rate somewhat lower than 100 % in the generation of single solitons. Second, the transition from a high duty-cycle extended pattern to a lower duty-cycle ensemble of one or several solitons comes with a dramatic drop in intracavity power that occurs on the timescale of the photon lifetime. If the resonator is in thermal steady-state before this drop occurs, the resonator will cool and the resonance frequency will increase. If this increase is large enough that the final detuning α exceeds $\alpha_{max} = \pi^2 F^2/8$, the soliton is lost. This challenge can be addressed by preparing initial conditions for soliton generation and then tuning to an appropriate point (α, F^2) before the cavity can come into thermal steady-state at the temperature determined by the larger power of the extended pattern; this is possible because the timescale over which an extended pattern can be generated is related to the photon lifetime, which is typically much faster than the thermal timescale.

The first report of soliton generation in microresonators came in a paper by Herr et al. published in 2014[27]. These authors described optimizing the speed of a decreasing-frequency scan of the pump laser across the cavity resonance so that a soliton could be condensed from an extended pattern and the scan could then be halted at a laser frequency where the soliton could be maintained, with the system in thermal steady-state at the temperature determined by the circulating power of the soliton. Other approaches for dealing with the challenges described above have been developed since this first demonstration; these include fast manipulation of the pump power [35, 37], periodic modulation of the pump laser's phase or power at f_{FSR}[8, 38], and tuning of the cavity resonance frequency using chip-integrated heaters instead of tuning the pump-laser frequency[**Joshi2016**, **Wang2018a**]. These methods continue to make use of extended patterns to provide initial conditions for soliton generation. In formally-equivalent fiber-ring resonators, direct generation of solitons without condensation from an extended pattern has been demonstrated using transient phase and/or amplitude modulation of the pump laser [39–41]. Chapter **??** of this thesis presents a new variation on these schemes that enables direct generation of solitons using only phase modulation at f_{FSR} without transient manipulation of the system parameters; this approach is based on a proposal by Taheri, Eftekhar, and Adibi [42].

Robust soliton crystals...

A variety of applications of soliton-based Kerr frequency combs have already been demonstrated. Some of these include demonstrations of an optical clock [43], dual-comb spectroscopy [**Suh2016**], coherent communications [**Marin-Palomo2018**], and direct on-chip optical frequency synthesis [6].

Science 354, 600

Nature 546 274

something else here

Chapter 3

PM Pumping

This chapter discusses the direct generation and control of single solitons in optical microring resonators using a pump-laser phase modulated at a frequency near the resonator's free spectral range. Based on a proposal by Taheri, Eftekhar, and Adibi in 2015 [42], these experimental results represent a promising new method for simple and deterministic generation of single solitons.

To illustrate the utility of using a phase-modulated pump laser, we first present theoretical investigations into the effect of this phase modulation (PM), and then we present experimental results on the generation and control of single solitons.

3.1 Theoretical investigation of soliton generation with a phase-modulated pump laser

To theoretically explore the physics of soliton generation with PM pumping, we use the LLE with a modified driving term that incorporates the effect of phase modulation [42]:

$$\frac{\partial\psi}{\partial\tau} = -(1+i\alpha)\psi + i|\psi|^2\psi - i\frac{\beta}{2}\frac{\partial^2\psi}{\partial\theta^2} + Fe^{i\delta_{PM}\cos\theta}. \tag{3.1}$$

Here δ_{PM} represents the phase-modulation index, where the resonator is driven by a field $E_{PM} = E_0 e^{i\delta_{PM}\cos(2\pi f_{PM} t)}$; $f_{PM} \sim f_{FSR}$ is the frequency of the applied phase modulation.

Simulations of Eq.3.1 reveal that PM transforms the resonator excitation spectrum from a series of $N = 0, 1, 2, ...$ up to N_{max} solitons to a single level $N = 1$ near threshold, eliminating degeneracy between these states as shown in Fig. 3.1. This occurs due to amplitude variations resulting from

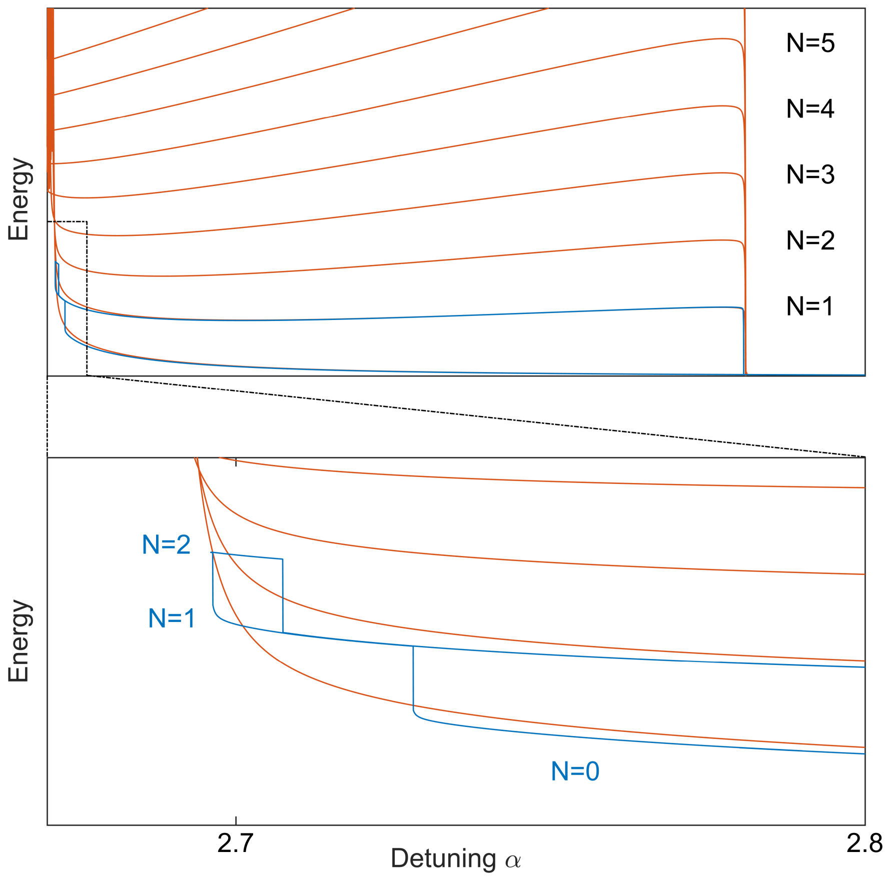

Figure 3.1: **title**text

the phase modulation, with dispersion and nonlinearity providing PM-to-AM conversion. We can gain some insight into the origin of this effect by inserting the ansatz $\psi(\theta, \tau) = \phi(\theta, \tau)e^{i\delta_{PM}\cos(\theta)}$ into Eq. 3.1 [40]. By expanding the second-derivative term and setting derivatives of ϕ to zero[1] we arrive at an equation for the quasi-CW background in the PM-pumped resonator:

$$F = (\gamma(\theta) + i\eta(\theta))\,\phi + i|\phi|^2\phi, \tag{3.2}$$

where effective local loss and detuning terms have been defined as:

$$\gamma(\theta) = 1 + \frac{\beta_2}{2}\delta_{PM}\cos\theta, \tag{3.3}$$

$$\eta(\theta) = \alpha - \frac{\beta_2}{2}\delta_{PM}^2\sin^2\theta. \tag{3.4}$$

[1] We note the contribution of Miro Erkintalo in suggesting this approximation.

This equation immediately yields an approximation for the stationary solution ψ_s:

$$\psi_s = \frac{F e^{i\delta_{PM}\cos\theta}}{\gamma(\theta) + i\left(\eta(\theta) - \rho(\theta)\right)}, \tag{3.5}$$

where $\rho(\theta) = |\phi(\theta)|^2$ is the (smallest real) solution to the cubic polynomial that results from taking the modulus-square of Eq. 3.2:

$$F^2 = \left[\gamma(\theta)^2 + \left(\eta(\theta) - \rho(\theta)\right)^2\right]\rho(\theta). \tag{3.6}$$

In neglecting spatial derivatives of ϕ but retaining the derivatives of the phase term $e^{i\delta_{PM}\cos\theta}$ we have made the approximation that the dominant effect of dispersion comes from its action on the existing broadband phase-modulation spectrum. This model reveals that amplitude variations in the quasi-CW background can be expected as a result of the spatially-varying effective loss and detuning terms that arise from the periodically-chirped pump laser.

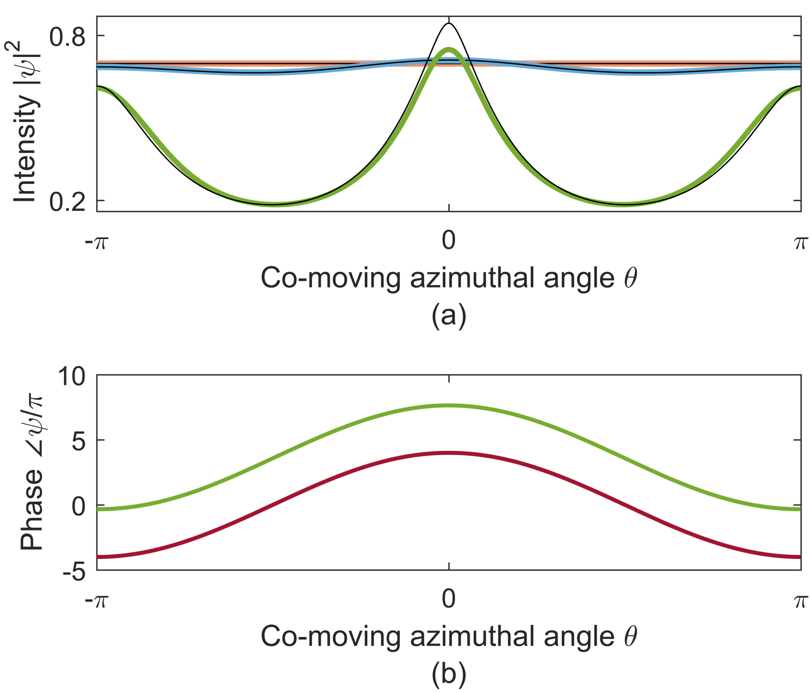

Figure 3.2: **title**text

Fig. 3.2 compares the predictions of numerical LLE simulations (color) with the analytical model (black). The two agree quantitatively at small modulation depth ($\delta_{PM} = \pi/2$, blue) and qualitatively at larger depth ($\delta_{PM} = 4\pi$, green). Both the simulations and the approximate analytic solution indicate that the background has two peaks per round trip in the presence of phase modulation, which suggests a mechanism for spontaneous single-soliton generation: At threshold the larger peak becomes locally unstable, and a soliton is formed by local modulation instability [41, 44]. Moreover, it is known that if solitons exist elsewhere they are pushed to the larger peak by the background's modulated phase [40]. This makes superpositions of $N > 1$ solitons unstable and practically forbidden. Generation of single solitons then simply requires tuning the pump power and frequency to appropriate values, regardless of initial conditions.

The detuning for soliton generation can be estimated using Eq. 3.2 by calculating the value of α where $\rho(\theta = 0) = 1$. This comes with a further approximation, as simulations reveal that the critical detuning for soliton formation is near but not necessarily at $\rho = 1$ because the spatial interval over which threshold is exceeded must have some minimum width. However, this approach quantitatively captures the behavior shown in Fig. 3.1, predicting soliton generation at $\alpha = 2.737$.

3.2 Spontaneous generation of single solitons using a phase-modulated pump laser

We demonstrate deterministic generation of single solitons without condensation from an extended pattern in a 22-GHz FSR silica ring resonator with $\Delta\nu \sim 1.5$ MHz linewidth [45]. We generate a frequency-agile laser for pumping the resonator by passing a CW laser through a single-sideband modulator that is driven by a voltage-controlled oscillator [46]; the seed laser is extinguished in the modulator and the resulting sideband can be swept by . The pump laser is phase-modulated with index $\delta_{PM} \sim \pi$ and amplified to normalized power F^2 between 2 and 6. We are able to measure and control the pump-laser detuning in real time using an AOM-shifted probe beam as shown in Fig. **??**, which allows thermal instabilities associated with the red detuning that is required for soliton generation to be overcome. The experimental setup and a frequency domain depiction of our locking scheme are shown in Fig. **??**.

rate and description here

To generate single solitons, we begin with large red detuning $\nu_0 - \nu_{pump}$ =40 MHz and decrease

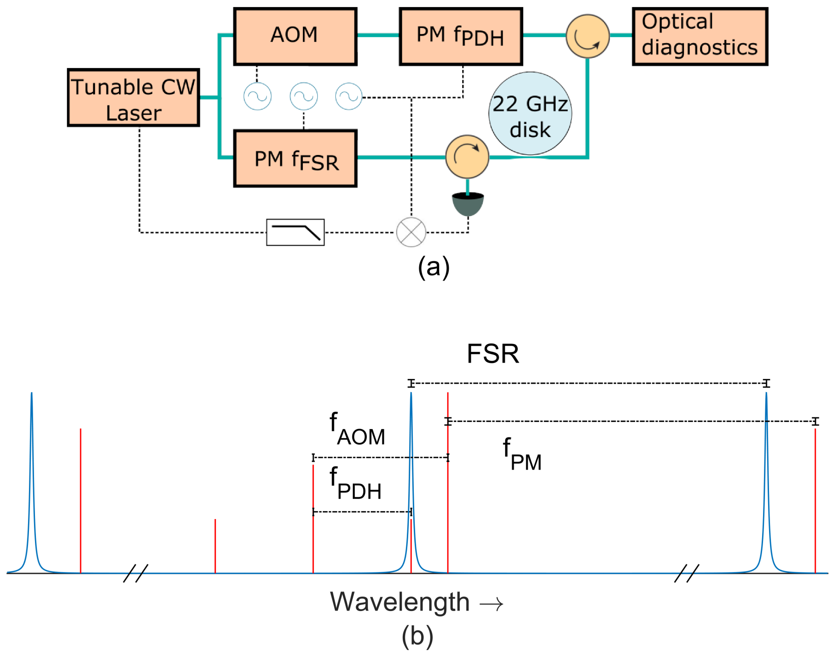

Figure 3.3: **title**text

the detuning until a soliton is generated near $\nu_0 - \nu_{pump}$ ~5 MHz detuning, where this value depends on the pump power and coupling condition. We measure the power converted by the Kerr nonlinearity to new frequencies by passing a portion of the resonator's output through an optical band-reject filter; this 'comb power' measurement reveals a step upon soliton formation, as shown in Fig. **??**. After soliton generation, we observe that the soliton can be preserved while the detuning is increased again up to a maximum value near , consistent with Fig. **??**. Additionally, we observe that it is possible to turn off the phase modulation without loss of the soliton, in agreement with the simulations presented in Ref. [42].

get from Jordan

Automating soliton generation by repeatedly scanning the laser into resonance ($\nu_0 - \nu_{pump}$ ~5 MHz) and back out again ($\nu_0 - \nu_{pump}$ ~20 MHz, far enough that the soliton is lost) has enabled reversible generation of 1000 solitons in 1000 trials over 100 seconds, with a measured 100 % success rate. Our probe beam allows measurement of the detuning at which soliton generation occurs, which changes little from run to run. We present a histogram of detuning measurements for the generation of 160 solitons in Fig. ??.

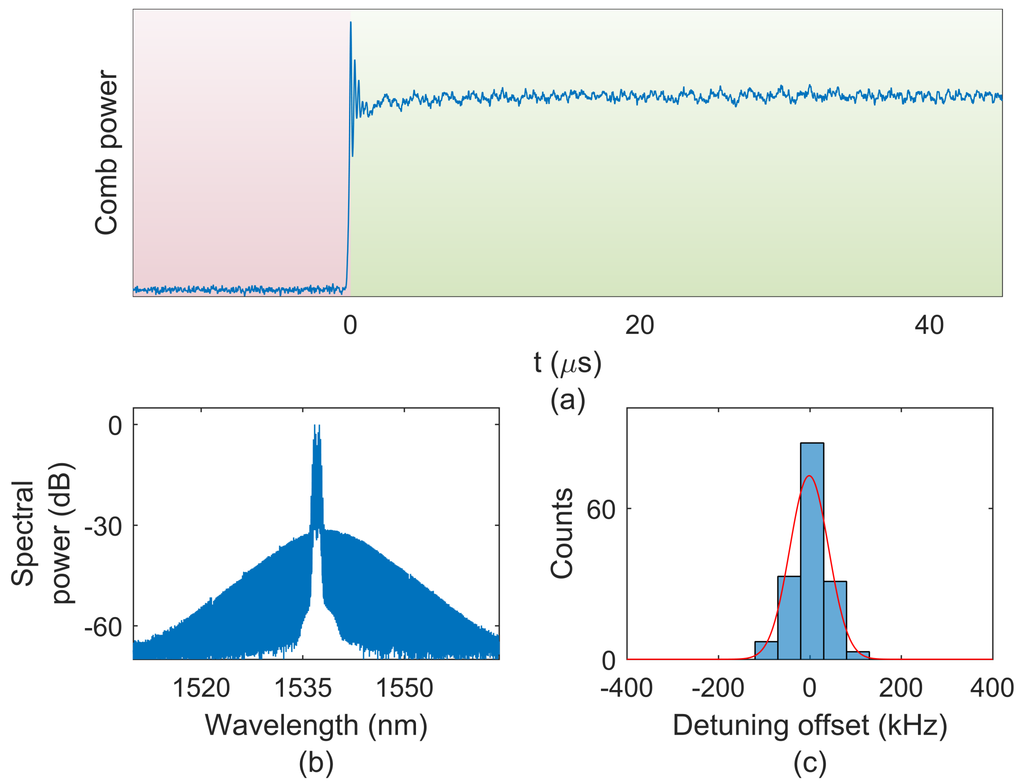

Figure 3.4: **title**text

3.3 Soliton control using a phase-modulated pump laser

In addition to enabling deterministic generation of single solitons, phase modulation of the pump laser also facilitates timing and repetition-rate control of the resulting pulse train. In our experiments, the repetition rate of the out-coupled pulse train (f_{rep}) remains locked to f_{PM} over a bandwidth of $\pm$40 kHz. This observation is consistent with an estimate of the locking range $\delta_{PM} \times D_2/2\pi \sim$44 kHz that is presented in Ref. [40], where we have used the approximate value $D_2 =$14 kHz/mode. Fig. ?? shows the measured repetition rate as f_{PM} is swept sinusoidally through a range of $\pm$50 kHz around the soliton's natural repetition rate; the repetition rate follows the PM except for glitches near the peaks of the sweep. In the inset of Fig. ?? we overlay the results of

LLE simulations that qualitatively match the observed behavior. These simulations are conducted by introducing the term $+\beta_1 \frac{\partial \psi}{\partial \theta}$ to the right-hand side of Eq. 3.1, where $\beta_1 = -2(f_{FSR} - f_{PM})/\Delta\nu$ incorporates a difference between the modulation frequency and the FSR of the resonator into the model; β_1 may be varied in time to simulate the sweep of f_{PM}. These simulations indicate that the periodic nature of the glitches is due to the residual pulling of the phase modulation on the soliton when the latter periodically cycles through the pump's phase maximum.

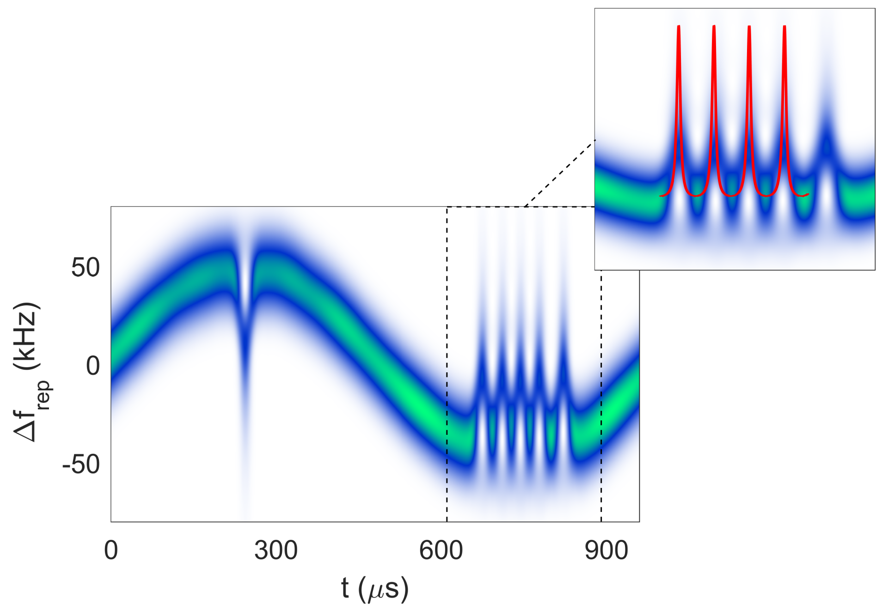

Figure 3.5: **title**text

To evaluate the utility of phase modulation for fast control of the soliton's properties, we measure the repetition rate of the pulse train as f_{PM} is rapidly switched ± 40 kHz, within the soliton's locking range. This measurement is conducted by photodetecting the pulse train after removing the central spectral lines corresponding to the spectrum of the pump laser using an optical band-reject filter. In order to obtain a measurement trace of the repetition rate as a function of time, the photodetected signal is split and one path is sent through a reactive circuit element that induces a frequency-dependent phase shift. By comparing the phase between the two paths as a function of time, the time-dependent repetition rate can be determined.

We construct eye-diagrams out of the resulting data; these are shown in Fig. **??**. In Fig. **??**,m

f_{PM} is switched with 200 μs period and 10 μs transition time; in Fig. **??** it is switched with 100 μs period and 60 ns transition time. These eye diagrams show that the PM enables exquisite control of the soliton pulse train.

We overlay a simulated eye diagram on the data in Fig. **??**. This simulation is conducted for parameters $\Delta\nu = 1.5$ MHz, $\delta_{PM} = 0.9\pi$ that are near the experimental values, and the agreement between measurement and simulation indicates that the measurements are consistent with fundamental LLE dynamics. Fig. **??** presents the results of additional LLE simulations; the basic result is that the switching speed of f_{rep} is limited by the resonator linewidth, and can be only modestly improved by increasing δ_{PM}.

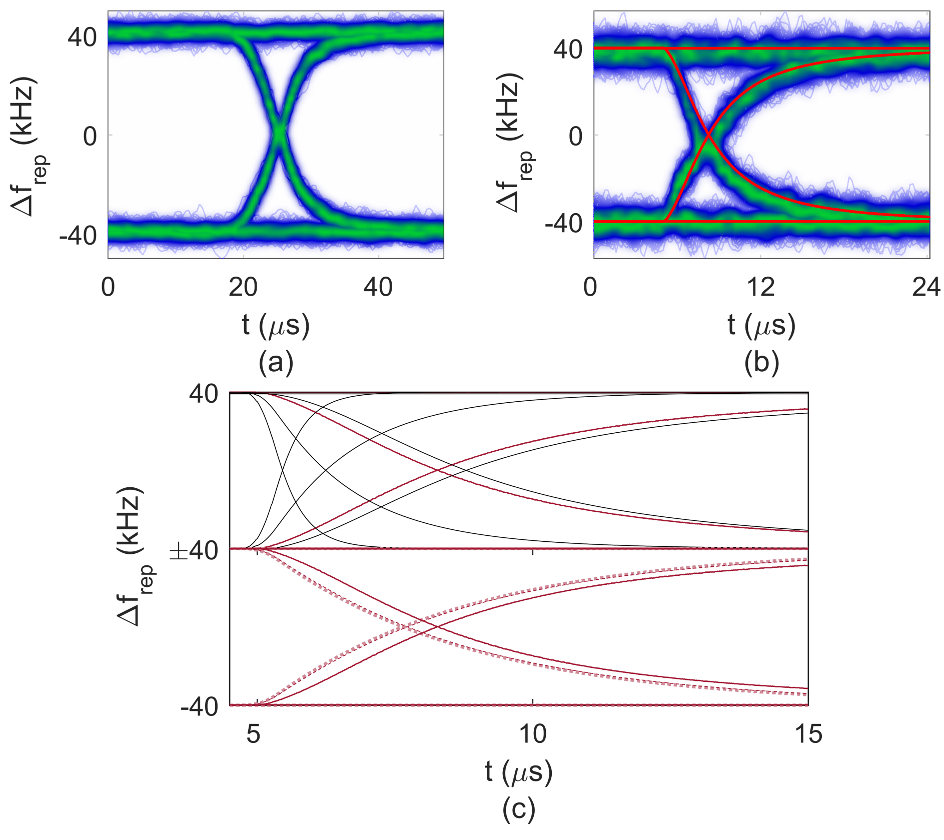

Figure 3.6: **title**text

3.4 Subharmonic phase modulation for high repetition-rate systems

One apparent barrier to the use of a phase-modulated pump laser for protected single-soliton generation and manipulation is the electronically-inaccessible FSRs of some typical microcomb resonators. However, it is possible to overcome this challenge by phase modulating at a subharmonic of the FSR. Simulations indicate that PM can directly excite single solitons with small modulation depth, e.g. $\delta_{PM} = 0.15\pi$. In this limit, only the first-order PM sidebands are relevant, and their amplitude and phase relative to the carrier control the dynamics. For a small desired modulation depth defined by the relationship between the first-order sidebands and the carrier, it is possible to modulate at a frequency $f_{mod} \sim f_{FSR}/N$ so that the N^{th}-order PM sidebands and the carrier address resonator modes with relative mode numbers -1, 0, and 1. The depth of modulation at the frequency f_{mod} can be chosen to fix the amplitudes of the N^{th}-order PM sidebands relative to the carrier and target a desired effective modulation depth. It is worth noting that when N is odd, phase modulation is recovered when the sidebands of order $-N$,0, and N address resonator modes -1, 0, and 1. When N is even the result is pure amplitude modulation, such that the driving term takes the form $F(1 + A\cos\theta)$. Simulations indicate that this AM profile also enables spontaneous single-soliton generation under some circumstances, but we note that this modulation profile cannot be obtained from a standard Mach-Zehnder modulator, which provides a drive like $F\cos(\eta+\delta\cos\theta)$.

Fig. **??** presents an example of this technique. We simulate spontaneous soliton generation with PM at $f_{mod} = f_{rep}/N = f_{rep}/21$. The effective modulation depth is 0.15π, which requires real modulation depth at the frequency f_{mod} with depth $\delta_{PM} \sim 8.3\pi$. Because the phase modulation spreads the optical power into the PM sidebands, use of this technique requires higher optical power for the same effective pumping strength; in this example the optical power must be increased by ∼15.6 dB. While the required modulation depth and pump power are higher with subharmonic phase modulation, neither is impractical. This technique could be used for spontaneous single-soliton generation in high-repetition rate systems; the example above indicates that it could be immediately applied in a 630 GHz-FSR resonator with 30 GHz phase modulation.

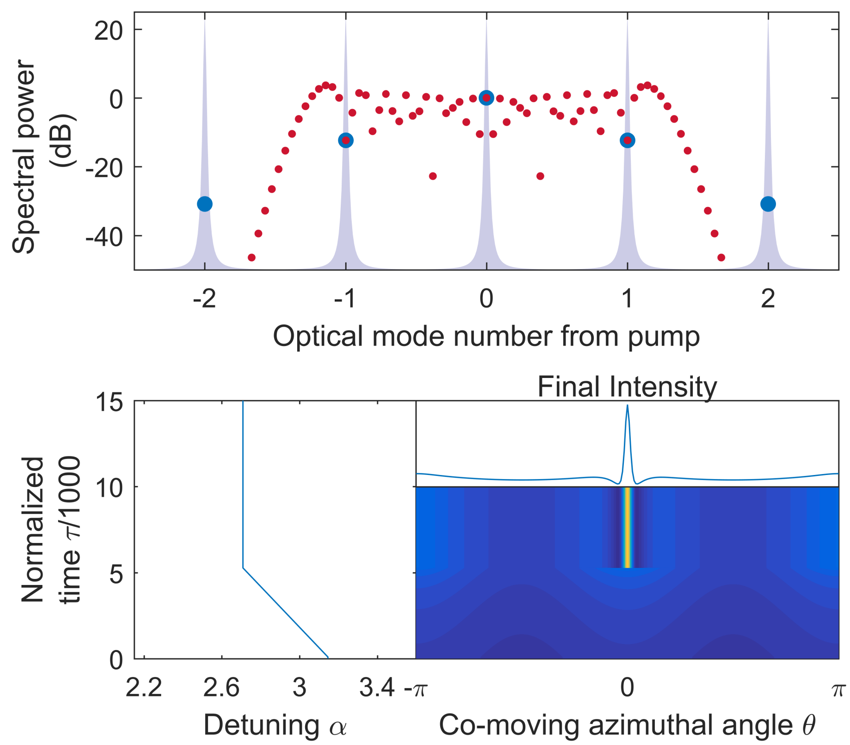

Figure 3.7: **title**text

Chapter 4

Soliton Crystals

This chapter presents results on the self-organization of ensembles of soliton in optical microring resonators. The reported phenomenon explains physics that goes beyond the basic LLE model of Kerr-comb formation, as is described in Sec. **??**. We refer to these self-organized ensembles as 'soliton crystals,' which extends an analogy to condensed-matter physics that has been made in other nonlinear-optical systems, including single-pass nonlinear fiber systems [47] and harmonically mode-locked fiber laser [48, 49], where a mechanism for soliton crystallization that is based on two distinct timescales of the laser medium [50] and is different from the one presented here was identified. Notably, the spatiotemporal chaos exhibited in the LLE was referred to as a 'soliton gas' in early studies of nonlinear dynamics in passive fiber-loop resonators [51–53].

Soliton crystals are soliton ensembles in which each soliton lies on a lattice site $\theta_n = 2\pi n/N$ in the co-moving frame, where N is the lattice parameter that arises from the fundamental physics of the system as described below and n indexes over the lattice sites. We have observed a wide variety of crystal configurations, and we present some of them in Sec. **??**; typically a small fraction of lattice sites are occupied by solitons. Soliton crystals are characterized by stable, dense occupation of the resonator by soliton pulses, and this dense occupation comes with high circulating power relative to single solitons or few-soliton ensembles. This important fact allows soliton crystals to be generated with decreasing pump-laser frequency scans across the resonance that are adiabatic in the sense that both the resonator temperature and the intracavity waveform are maintained at the values[1] that

[1] something about chaos

would be expected from the instantaneous α and F^2 parameters throughout the scan.

We demonstrate generation of a soliton crystal in Fig. 4.1; it is useful to contrast this with the behavior exhibited in Fig. **??**.

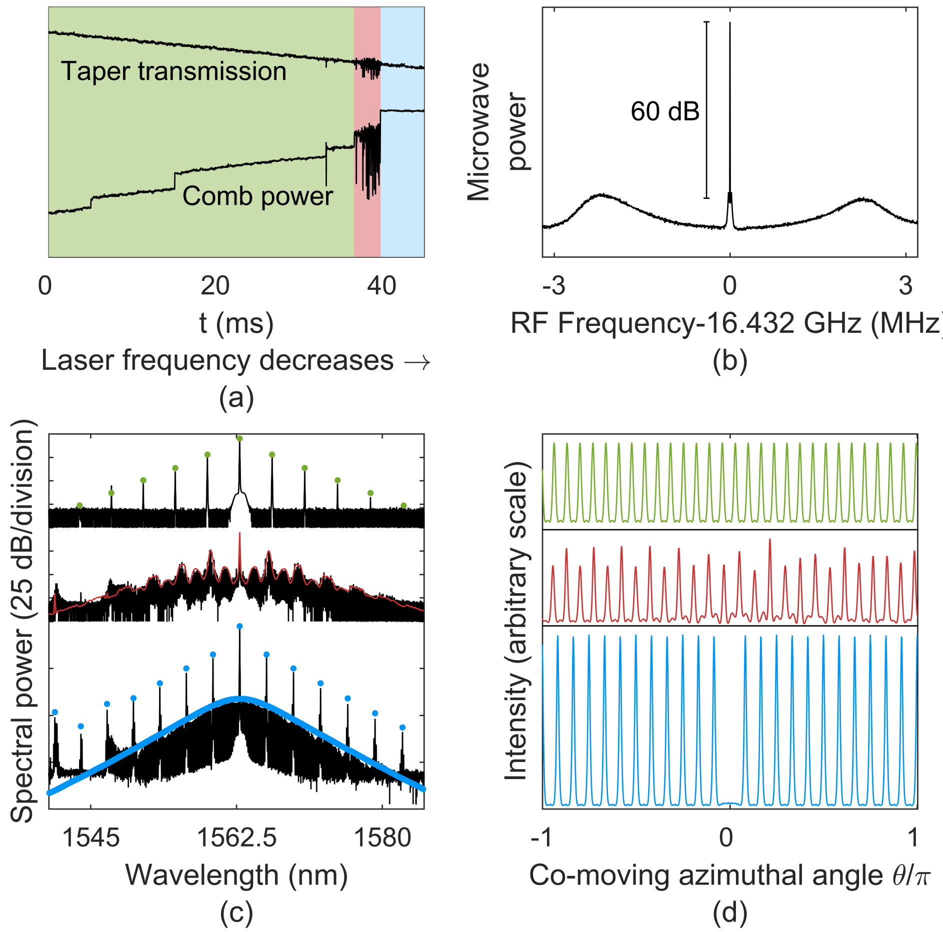

Figure 4.1: **title**text

4.1 Mechanism of soliton crystallization

Fig. 4.1 presents the optical spectrum and corresponding time-domain simulation of a soliton crystal. This spectrum consists of widely-spaced primary-comb lines that are separated by many resonator FSR, superposed on top of an underlying sech^2 spectrum of the kind that corresponds to a single soliton. In fact, this spectrum can be understood through the basic superposition principle of the electric field: The primary comb spectrum with spacing $N \times f_{FSR}$ corresponds to a train of N uniformly spaced pulses in the resonator. The observed crystal spectrum corresponds to such a pulse train with a single vacancy, where a pulse is missing. The effect of this vacancy on the spectrum can be understood by considering the addition of an *out-of-phase* pulse to the pulse train that coincides in time with one of the existing pulses—in the time domain this corresponds to removal of one of the pulses, while in the spectral domain this corresponds to the addition (in the phase-sensitive field quantity) of the primary-comb spectrum and the single, out-of-phase soliton.

The simulated time-domain waveform of the soliton crystal presented in Fig. **??** is not stable in evolution under the LLE. The observed width of the spectrum fixes the ratio between α and β, as seen from Eq. 2.20. This ratio then fixes the temporal duration of the solitons, in turn determining the characteristic length of their interactions. When an attempt to simulate the crystal according to the LLE is made with parameters $\alpha =$?? and $\beta =$?? that give agreement with the measured width of the optical spectrum, it is found that pair-wise attractive interactions between solitons lead to collapse of the crystal.

A stabilization mechanism that goes beyond the physics of the LLE is responsible for the stability of this and other soliton crystals. The stabilization mechanism arises from avoided mode-crossings in the resonator spectrum. A 'mode family' corresponds to a set of circulating modes that have different azimuthal mode numbers but (approximately, neglecting wavelength-dependent effects) the same transverse spatial mode profile. As discussed in Sec. **??**, some resonators support multiple mode families, each with its own free spectral range at a given wavelength. Although the modes in different families are in principle orthogonal, coupling between them can be provided, for example, by the coupling waveguide or tapered fiber used to drive the resonator. If a coupling exists between two modes that are sufficiently close in frequency, the frequencies of the modes become displaced from their frequencies in the absence of this coupling [**Haus1991**]. This affects Kerr-comb generation in the affected mode families, because the local detuning between the resonator modes and the Kerr-comb modes is changed as a result of the mode crossing. This comb-resonator detuning change may either enhance or inhibit nonlinear frequency conversion to the effected Kerr-comb modes, thereby changing the amplitude of these modes in the comb spectrum.

It has been reported that avoided mode crossings in the resonator spectrum can inhibit soliton generation in anomalous-dispersion resonators[**4**, **6**], while they can facilitate the formation of Kerr-combs in normal-dispersion resonators[**37**] . Here we are interested specifically in the impact of the avoided mode crossing on the waveform of a soliton. For simplicity, we focus on the case where a single comb mode is affected by the mode crossing. When the change in the comb-resonator detuning increases the amplitude of that mode in the soliton's spectrum, the change to the time-domain waveform can be understood by considering this increase as the addition of extra CW light at the frequency of that mode. This extra CW light exists throughout the cavity, and it leads the introduction of periodic intensity oscillations in the background on which the soliton rides as the new CW light beats against the existing background at the pump frequency. This new background wave in the cavity has a period of $2\pi/\mu_\times$ in the angular coordinate θ, where $\mu_\times$ is the pump-referenced mode number of the Kerr-comb mode affected by the mode crossing, for which the detuning has been shifted.

other citations here

When several of these perturbed solitons co-propagate in a resonator, they interact through their extended waves and arrange themselves such that the waves constructively interfere. Each soliton then lies at the peak of a single extended background wave in the resonator, similar to predictions for bichromatically pumped Kerr combs[**38**]. Importantly, temporal separations between solitons are therefore required to be multiples of this wave's period, and the wave stabilizes the crystal against the attractive interactions discussed above. Furthermore, the wave's amplitude, and thus the strength of the crystal against perturbations, increases with the number of co-propagating perturbed solitons. Finally, we note that at least within the assumption of single-mode perturbation of the comb's spectrum, this interaction has infinite range.

We note that the mechanism observed here builds on previous reports of related phenomena. It has been shown that local interactions between cavity solitons can arise through decaying oscillatory tails [**39**], leading to the formation of small, locally ordered soliton molecules. Furthermore, it has been shown that the injection of an additional CW laser into a passive fiber-ring resonator can result in the generation of uniform distributions of solitons [**40**]. The mechanism we report here can be viewed as a variant of this CW-soliton interaction in which the 'injected' CW laser is provided by the affect of the mode crossing on the solitons' spectra.

We connect this discussion to the soliton-crystal spectrum presented in the bottom trace of Fig. 4.1c—this spectrum exhibits excess power near pump-referenced modes numbers $\mu_{\times,1} = 5\times 24 = 120$ (1,547 nm) and $\mu_{\times,2} = 7 \times 24 = 168$ (1,541 nm). Also visible is suppressed comb generation where the comb-resonator detuning has been increased. Here 24 FSR is the spacing of the prominent primary-comb lines.

4.1.1 Simulation of soliton crystals

To incorporate the stabilization mechanism described above into numerical simulations, we incorporate into the LLE a reduced comb-resonator detuning on a single mode $\mu_\times$. The mode-dependent comb-resonator detuning can be calculated as:

$$\alpha_\mu = -2(\Omega_0 - D_1 + \omega_\mu)/\Delta\omega, \tag{4.1}$$

$$= \alpha - \beta\mu^2/2. \tag{4.2}$$

Here Ω_0 is the frequency of the pump laser, ω_μ is the set of cavity resonance frequencies referenced to the pumped mode, and $D_1 = \partial\omega_\mu/\partial\mu|_{\mu=0}$ is the resonator's FSR at the pumped mode and is also assumed to be the Kerr-comb's repetition rate. The dispersion operator is applied in the frequency domain in numerical simulations of the LLE (see **??**), which facilitates inclusion of δ-function perturbations to the comb-resonator detuning as:

$$\alpha_\mu = \alpha - \beta\mu^2/2 + \Delta\alpha_\mu, \tag{4.3}$$

where

$$\Delta\alpha_\mu = 2(\omega_\mu - \omega_{\mu,0})/\Delta\omega \tag{4.4}$$

is the normalized change in the frequency of mode μ from the expected frequency $\omega_{\mu,0}$.

We demonstrate the stabilization mechanism and the simulation method by presenting a simulation of the crystal in Fig. 4.1c. The simulation is shown in Fig. **??**. This figure illustrates that, without the stabilization mechanism, the crystal will collapse. We note that a phenomenological application of coupled-mode theory[**Haus1991**] could be used to calculate the full perturbation to the soliton spectrum by the mode crossing, but we find that to explain the existence of this 23-soliton crystal and the apparently exact circumferential spacing of the pulses by $2\pi/24$ radians, it is sufficient to incorporate into the LLE a reduced comb–resonator detuning on only mode 120 or on mode 168, where the excess power is largest. The crystal is then a steady-state solution of the resulting perturbed LLE.

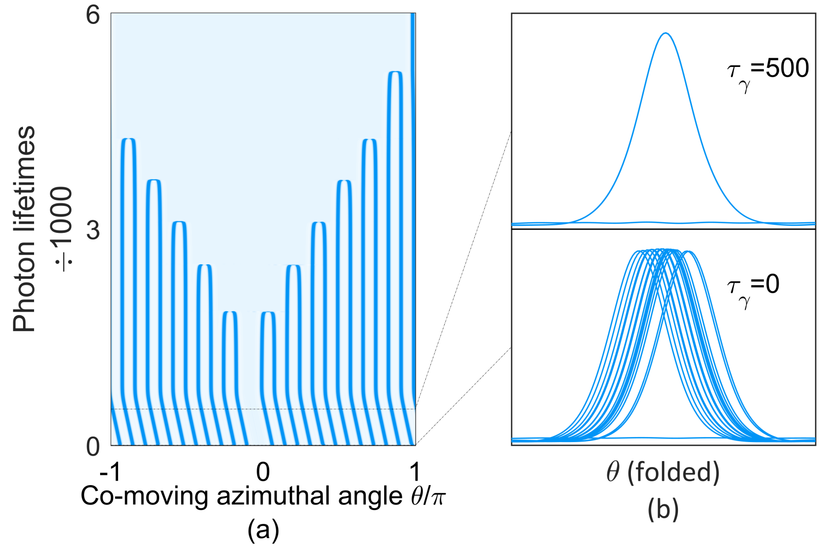

Figure 4.2: **title**text

4.2 Case study: superstructured crystal

We consider a second specific example of a soliton crystal. The measured optical spectrum for this crystal is shown in Fig. 4.3a. This crystal exhibits superstructure—the soliton pulse train isnearly periodic in a small unit cell but is modulated with a larger periodicity. This rseults from the frustrated uniform distribution of 16 solitons with allowed inter-soliton separations of $2\pi n/49$ radians; one pair is spaced by $4\times2\pi/49$ instead of $3\times2\pi/49$ radians. Excess power is apparent in the spectrum at mode $\mu_\times = 49$ (highlighted by the red circle in the plot), and we simulate this crystal by phenomenologically reducing the comb-resonator detuning on mode 49 so that the experimental and simulated spectra agree. The background wave resulting from the constructive interference of the extended waves of the solitons, each having an angular period of $2\pi/49$, is visible in the plots of the simulated intensity in Fig. 4.3b and c.

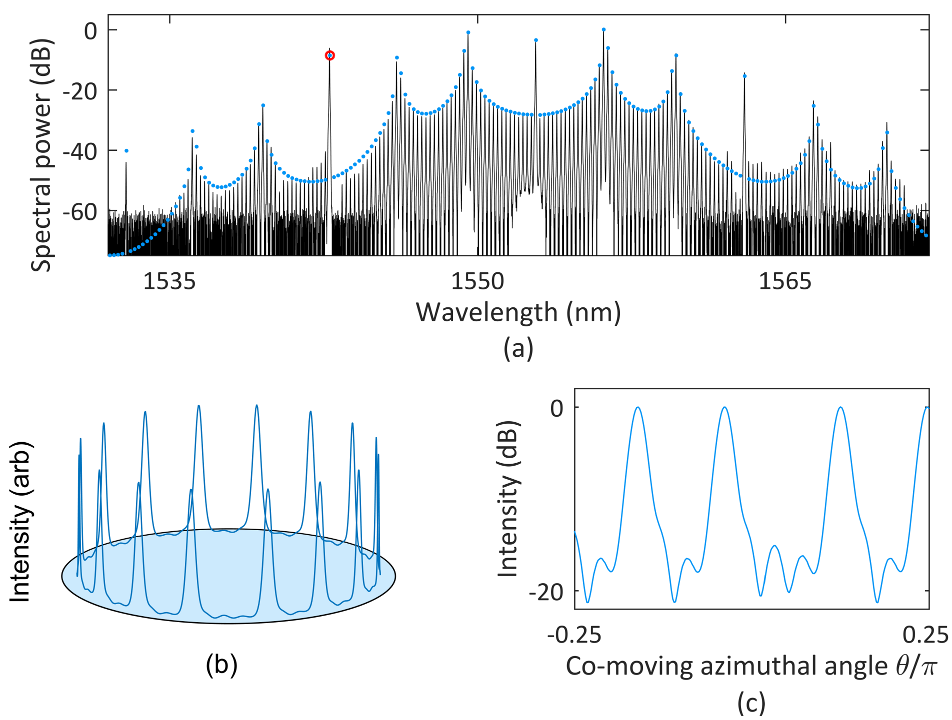

Figure 4.3: **title**text

To gain insight into crystal generation, we simulate laser frequency scans across the resonance that generate this crystal in the presence of the mode crossing on mode 49. Example scans are shown for the case without the mode crossing (green) and with it (blue) in Fig. 2d. In both scans, solitons emerge from chaos as the frequency of the laser is decreased. In the presence of the mode crossing, they are generated with inter-soliton separations of $2\pi n/49$ radians. A greater number of solitons emerge from chaos in the presence of the mode crossing, and this higher number helps to stabilize the crystal against thermal changes in the experiment. Further, upon continuation of the simulation, some of the solitons in the scan without the mode crossing interact attractively and pair-annihilate, while the crystallized ensemble resulting from the scan with the mode crossing remains stable indefinitely.

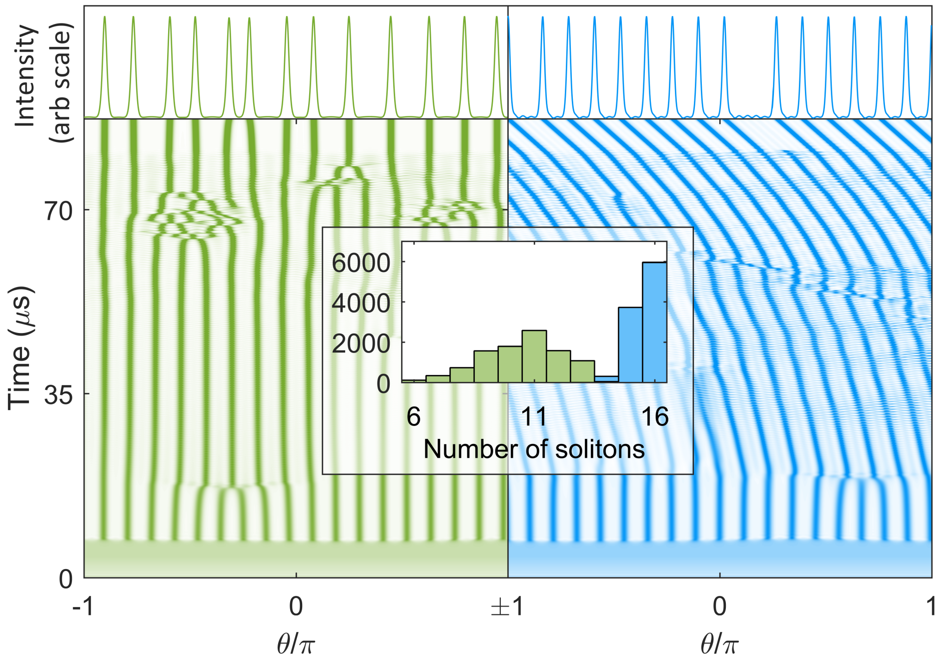

Figure 4.4: **title**text

We investigate the pair-distribution function (PDF) for the soliton ensembles generated by these scans. The PDF is the probability that a soliton exists at position $\theta_0 + \Delta\theta$ given that a different soliton exists at position θ_0, normalized to the density. This is a useful metric to classify particle interactions which we borrow from condensed matter physics (see e.g. Ref. [**42**], especially Fig. 2, and Ref. 43, especially Fig. 1.1 and Chapter 3). We note that for numerically calculated discrete PDFs the absolute scaling of the PDF is not important, as it depends on the density of numerical sampling. In Fig. 2e, we plot the average PDFs for 10000 simulated scans with and without the mode crossing. The result for the case with a mode crossing is sharply peaked, indicating that the allowed inter-soliton separations take on discrete values. The result for the case without the mode crossing is continuous, with a peak near the most likely nearest-neighbour separation and periodic revivals at its multiples, falling to the value of the PDF for uncorrelated soliton positions (the density) at large separations. This is exactly the expected form of the PDF for a liquid [**42**,

43]. For comparison, we plot a PDF (black, Fig. 2e) generated by simulation of a simple particle ensemble with mean inter-particle separation of $\Delta\theta = 0.155\pi$ and normally distributed noise on this value with standard deviation of $\sigma_{\delta\theta} = 0.18\Delta\theta$. Thus, with a particle labelled by $n = 0$ fixed at $\theta = 0$, the position of particle n is $\theta_0 = n\Delta\theta + \Sigma_n \delta\theta_i$, with $\delta\theta_i$ the instantiations of the random variable representing the noise on the pulse spacings.

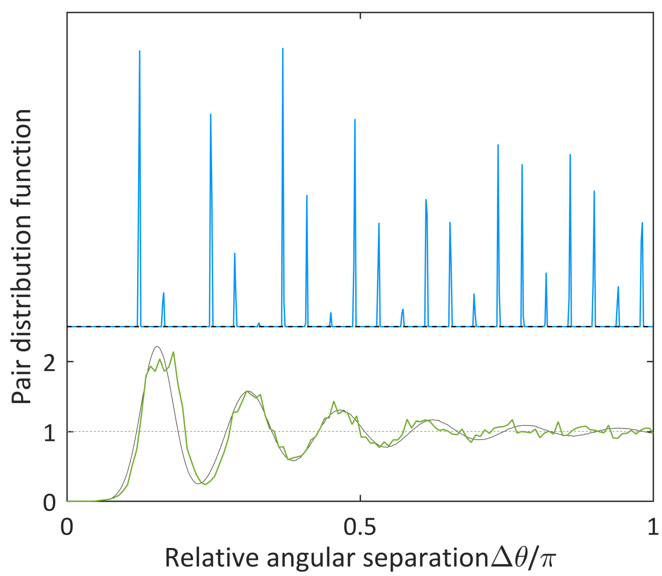

Figure 4.5: **title**text

4.3 Soliton crystal configuration space

We observe a rich variety of soliton crystals explained by ordering in accordance with an extended background wave as described above; many of the optical spectra are plotted in Fig. 3. Operationally, we adjust the pump laser power to provide repeatable conditions for creating particular crystals; more complex crystals occur with increased laser power, which intensifies the fluctuations in the chaos that precedes crystal generation and provides less well-ordered initial conditions. Once a crystal is generated, it is stable to small adjustments in the pump power and detuning, as the crystal structure is determined by the initial conditions for soliton formation rather than by an explicit dependence on pump power or detuning. The crystals we observe exhibit vacancies (Schottky defects)[**27**], Frenkel defects[**27**], disorder, or superstructure, or some combination thereof. A Frenkel defect consists of the shifting of a soliton in an otherwise uniform crystal. Disordered crystals are crystals in which the solitons fall on the peaks of the extended background wave, but their distribution across these peaks varies without any apparent regular order or favoured period.

We highlight the crystal plotted in Fig. 3n. This crystal exhibits both superstructure, with a superlattice period of $2\pi/3$ radians, and a Frenkel defect. Three identical supercells per resonator round-trip yield a spectrum which has light in optical modes spaced by three resonator FSR, because the waveform's period has been reduced threefold. The Frenkel defect, occurring once per round-trip, contributes the single-FSR lobes to the spectrum. The result is three bursts of 8, 9, and 10 solitons respectively.

Fig. 3o shows a soliton crystal with inter-soliton separations that are slightly irregular and which we have not simulated as a steady-state solution of any perturbed LLE. We expect that the formation of the crystal and the distribution of solitons are dictated by mode interactions, but that in this case our simple approximation of a perturbation to the LLE by a reduced comb-resonator detuning on a single comb mode is not appropriate. Finally, we highlight the series of crystals plotted in Figs. 3p-3t. This series of crystals was generated by moving the pump laser closer to a mode-crossing in steps of integer multiples of the resonator FSR. This data demonstrates the influence of the background beating between the pump laser and the mode-crossing in determining the configuration of solitons in the resonator.

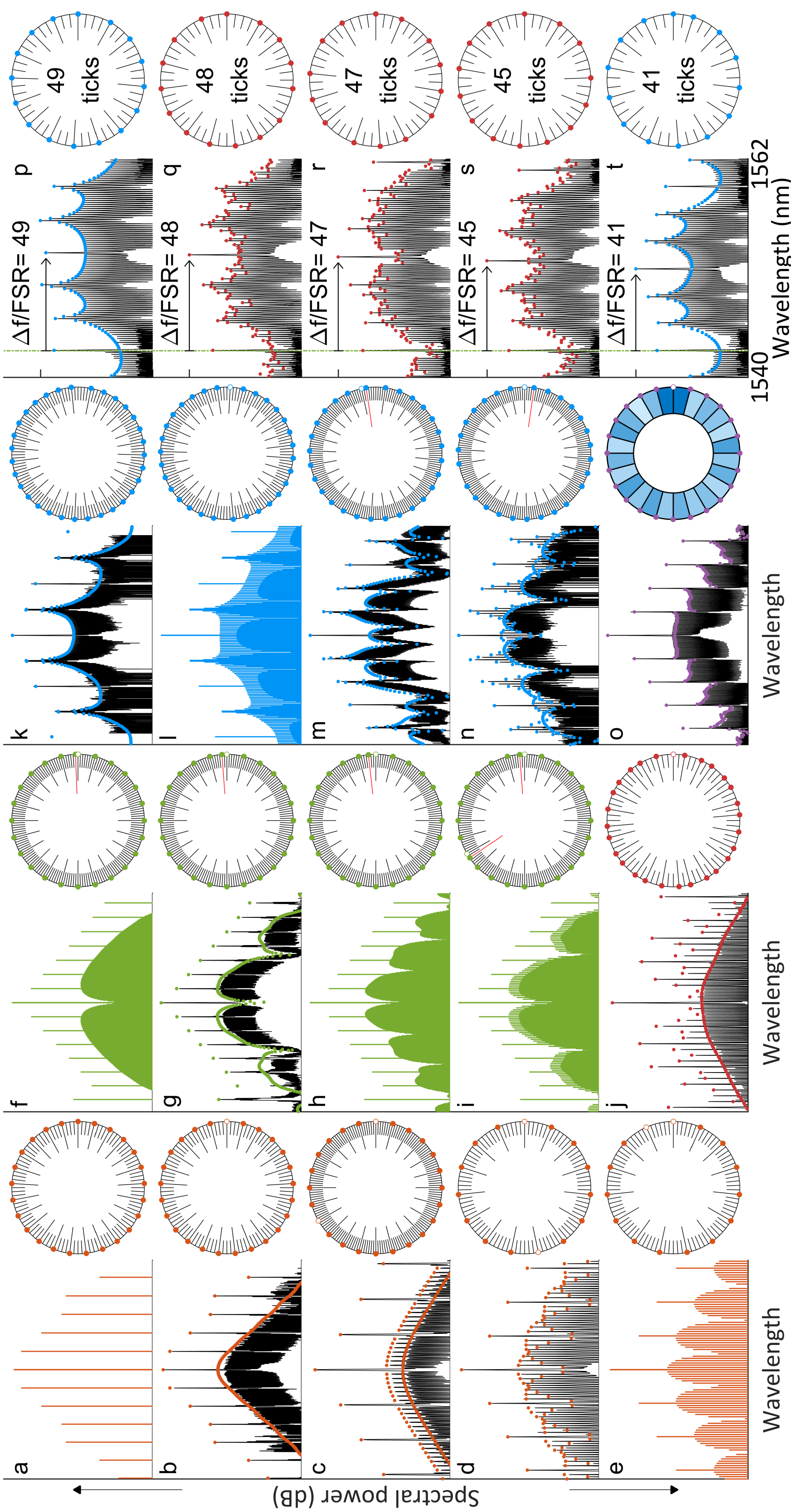

Figure 4.6: **title**text

Chapter 5

EOM Combs

In this chapter, I discuss the generation of high-repetition-rate frequency combs through electro-optic modulation of a continuous-wave laser – so-called EOM combs [54–63]. This scheme represents an alternative to parametric generation of HRR combs in Kerr resonators, and as the technology matures it will likely find a niche in the application space that leverages its long-term stability, lack of moving parts, and possibility for robust turn-key operation. First I present the operational principle, and then experimental results that represent the first generation of a coherent octave-spanning supercontinuum and detection of an active-modulation-based frequency comb's carrier-envelope offset frequency without an external optical reference. Then I provide a detailed discussion of the noise properties of the EOM comb, the investigation of which is a significant contribution of the work described here. Finally, I provide a discussion of some possible future directions for the technology.

5.1 Principle of operation

Generally, the EOM comb concept consists of passing a CW 'seed' laser through cascaded phase and intensity modulators to generate a train of chirped pulses, and then propagating this pulse train through a dispersive medium to temporally compress the pulses to near their bandwidth-limited pulse duration. An generic expression for the electric field before temporal compression results from the product of the field $E_o e^{-i\omega_c t}$ with operators

$$\frac{1}{2}\left\{\exp\left[i(\phi_{DC}+\phi_{RF}\sin\omega_r t)\right]+\exp\left[-i(\phi_{DC}+\phi_{RF}\sin\omega_r t)\right]\right\} \tag{5.1}$$

$$=\cos\left(\phi_{DC}+\phi_{RF}\sin(\omega_r t+\phi_{IM-PM})\right) \tag{5.2}$$

representing the intensity modulation and

$$\exp\left[i\beta_m\sin\omega_r t\right] \tag{5.3}$$

representing the phase modulation. Here E_o and ω_c are the complex amplitude and the carrier frequency of the seed laser. The phases ϕ_{DC} and ϕ_{RF} represent the DC bias and depth of the intensity modulation, respectively, which experimentally are sourced from a DC power supply and an RF synthesizer. Writing the intensity-modulation operator as the sum of exponentials reveals the physical origin of intensity modulation as phase modulation in two paths with opposite sign. The phase-modulation index, which sets the initial bandwidth of the EOM comb, is β_m. The comb's repetition rate is $f_r = \omega_r/2\pi$, with ω_r the angular frequency of the phase and intensity modulation, which in practice are derived from the same synthesizer. The phase ϕ_{IM-PM} represents a phase difference between the IM and PM operators arising from path-length differences, which can be controlled via the insertion of a phase shifter in one electrical path.

In practice, for subsequent spectral broadening of the comb it is desirable to configure the IM and PM to yield a train of 50 % duty-cycle pulses with normal chirp (temporally increasing carrier frequency). To achieve this, both ϕ_{DC} and ϕ_{RF} are set to $\pi/4$ and ϕ_{IM-PM} is set to zero. To achieve the former, the DC bias voltage and the RF modulation amplitude are adjusted to yield the appropriate optical spectrum for the seed laser with only intensity modulation applied. Setting ϕ_{IM-PM} to either zero or π is achieved by examining the optical spectrum of the EOM comb with both IM and PM applied. The spectrum is asymmetric if ϕ_{IM-PM} is not zero or π due to stronger transmission of either the high- or low-frequency components of the phase-modulated seed laser through the intensity modulators. The optical spectrum of the comb, which does not include phase information, is the same for $\phi_{IM-PM} = 0$ or π; the difference between the two corresponds to reversal of the field in time or, equivalently, the difference between normal and anomalous chirp. In practice, setting ϕ_{IM-PM} to zero can be achieved by verifying that the pulses are compressed by propagation in an appropriate length of an anomalously dispersive medium; $\phi_{IM-PM} = \pi$ corresponds to anomalous chirp.

A simplified and illuminating expression for the electric field of a normally-chirped 50 % duty-cycle pulse train (up to a constant overall phase shift relative to the previous expression) is:

$$E = E_o \cos\left(\frac{\pi}{2}\sin^2\frac{\omega_r t}{2}\right) e^{i\omega_c t - i\beta_m \cos\omega_r t}. \tag{5.4}$$

This can be understood as the product of a time-varying real amplitude $a(t) = E_o \cos\left(\frac{\pi}{2}\sin^2\frac{\omega_r t}{2}\right)$ and a phase factor from which the instantaneous carrier frequency $\omega(t) = \omega_c + \omega_r\beta_m \sin\omega_r t$ can be calculated. The carrier frequency $\omega(t)$ is increasing when the amplitude $a(t)$ is at its maximum, corresponding to normal chirp on the pulses.

5.2 Detection of the carrier-envelope offset frequency of an EOM comb

Here I describe generation of an EOM comb with 10 GHz repetition rate and subsequent measurement of its carrier-envelope offset frequency. The experimental setup is depicted in Fig. 1a. The basic experimental scheme consists of the following steps: 1. Initial generation and temporal compression of the EOM comb pulse train; 2. Modest spectral broadening and temporal re-compression; 3. Noise reduction using a Fabry-Perot filter cavity; and 4. Octave-spanning supercontinuum generation and detection of the carrier-envelope offset frequency. The results described below represent the first time a frequency comb based on active modulation of a CW laser has been self-referenced. Key to the success of this approach is the implementation of nonlinear spectral broadening in two stages, which allows the second stage to be seeded with ∼130 fs pulses for coherent supercontinuum generation. The noise reduction stage is also critical for coherent spectral broadening, and the investigation of its effects is a significant contribution of this work.

To generate the initial train of chirped pulses, a telecom-band continuous-wave laser is passed through cascaded phase and intensity modulators driven with a 10 GHz microwave signal. The intensity modulator is biased at the 50 % transmission point and driven with an RF amplitude appropriate for generation of a 50 % duty-cycle pulse train, as described above. The phase modulator is driven with modulation depth of $\sim 31\pi/4 \sim 24.3$ rad. The relative phase between the modulators is set such that the phase applied by the phase modulator is at a minimum when the transmission of the intensity modulator is highest; this yields a train of normally-chirped (up-chirped) pulses. Simulated temporal intensity and instantaneous carrier-frequency profiles are shown in Fig. 1b, and a simulated optical spectrum is overlaid on an experimental measurement in Fig. 1c.

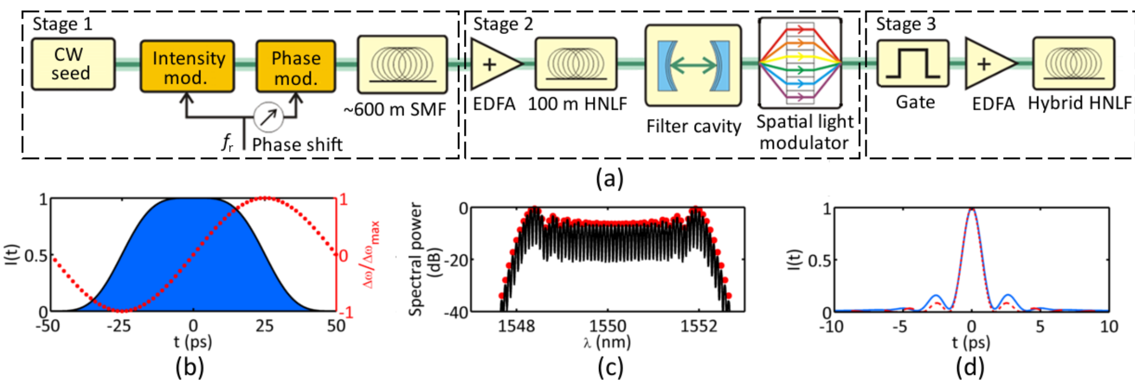

Figure 5.1: **Schematic and principle of operation for detection of the carrier-envelope offset frqeuency of an EOM comb.** (a) Experimental schematic for f_0 detection, with three stages: 1. Initial generation and temporal compression of the pulse train; 2. First stage of spectral broadening and temporal re-compression, along with noise suppression, and 3. Final stage of spectral broadening for generation of a coherent octave-spanning supercontinuum, including the implementation of an electro-optic gate for repetition-rate downsampling. (b) Depiction of a constituent pulse from a train of 50 % duty-cycle normally-chirped pulses with 10 GHz repetition rate. Intensity is shown in blue, and instantaneous carrier frequency is shown in red. The periodic electric field of this pulse train is given by Eqn. **??** (c) Measured optical spectrum of the initial EOM comb pulse train (black), along with the simulated spectrum corresponding to the plots in panel (b). (c) Simulated temporal compression of the pulses shown in panel (b), with compression conducted by propagation in 570 m of SMF (solid blue) and compression to the transform limit (dashed red). The full-width at half-maximum (FWHM) duration of both pulses is ~1.5 ps.

Next, the chirped pulse train is propagated through 600 m of anomalously-dispersive SMF. The length of SMF that is appropriate for pulse compression depends on the bandwidth of the optical pulses to be compressed; equivalently, it depends on both the phase-modulation depth and the repetition rate of the pulse train. This temporal compression reduces the duration of the optical pulses from ~50 ps to $\sim$ 1.5 ps. A simulation of the resulting intensity profile is presented in Fig. 1d.

The compressed pulses are amplified to 400 mW average power in an erbium-doped fiber amplifier and launched into 100 m of HNLF. This section of HNLF has chromatic dispersion that is small and normal; this is carefully chosen to chirp the pulses via self-phase modulation while avoiding soliton-fission dynamics[64]. The result is a train of chirped $\sim$1.5 ps pulses exiting the fiber. In Fig. 2a we present the measured optical spectrum of this pulse train, as well as results of a numerical simulation of the spectral broadening in the 100 m of normally-dispersive HNLF. These simulations are conducted using the nonlinear Schrodinger equation (NLSE) including third order dispersion[15], taking as initial conditions the calculated intensity profile of the EOM comb pulses shown in Fig. 1d. The dispersion values for the HNLF used in the simulation are $D = -0.04$ ps/nm·km and $D' = 0.003$ ps/nm^2·km, close to the values specified by the manufacturer. The simulation method is described in detail in App. **??**.

After propagation through the first section of HNLF, the pulses are passed through a high-finesse Fabry-Perot cavity for suppression of optical frequency fluctuations as discussed below. Then the pulses are temporally compressed again, this time using a commercial spatial light modulator (SLM) [65]; the SLM separates narrow spectral regions using a grating and passes them through individually controlled delaying elements before recombination. The SLM applies 2$^{\text{nd}}$, 3$^{\text{rd}}$, and 4$^{\text{th}}$ order chromatic dispersion, which simulations indicate is sufficient to compress the chirped pulses to $\sim$130 fs, near their transform limit. This is shown in Fig. 2b. While it is convenient, the SLM is not strictly necessary; it would also be possible to compress the pulses via propagation in an appropriate length of SMF. Figs. 2b and 2c present the output intensity profile and the evolution of the intensity profile, respectively, in simulated compression in SMF. Because the pulses are broadband, temporally short, and reasonably high energy, these simulations include the full dispersion profile of SMF and the Kerr nonlinearity.

The temporally compressed $\sim$130 fs pulses are then passed through a Mach-Zehnder modulator functioning as an electro-optic gate for repetition-rate downsampling (see Chapter 6). The gate selectively transmits every fourth pulse, reducing the repetition rate of the pulse train to 2.5 GHz. This facilitates coherent supercontinuum generation in a second stage of spectral broadening by increasing the pulse energy that can be achieved at a given average power. Note that this step is convenient but not strictly necessary, as shown in Ref. [66].

The downsampled 2.5 GHz pulse train is amplified to an average power of 1.4 W, resulting in a train of $\sim$0.56 nJ pulses. This pulse train is propagated through 8 m of hybrid HNLF, yielding the spectrum shown in Fig. 2d. This hybrid HNLF consists of two segments with different dispersion profiles, with each segment serving a different purpose. The first segment is 30 cm long and highly dispersive ($D = 6$ ps/nm·km), and generates a dispersive wave centered at 1090 nm. The second segment is 7.7 m long and has lower dispersion ($D = 1.5$ ps/nm·km), and generates a Raman-self-frequency-shifted soliton centered near 2150 nm. The effect of each of these fibers on the output spectrum can be understood by investigating propagation in each section separately. To do this we use the LaserFOAM program [67], which employs the generalized NLSE including Raman scattering, self-steepening, and 2nd- through 4th-order dispersion. The simulations are run independently, and both take as their initial conditions 170 fs Gaussian pulses with 350 pJ energy, close to the energy coupled into the HNLF after accounting for losses. The results of these simulations are plotted in Fig. 2d.

The supercontinuum generated in the hybrid HNLF is coherent and suitable for $f - 2f$ self-referencing (see App. **??**). To detect the carrier-envelope offset frequency of the EOM comb, we pass the pulse train through an interferometer consisting of a dichroic mirror, a delay stage in one path, and a 10 mm sample of periodically-poled lithium niobate that generates the second harmonic of supercontinuum light at 2140 nm. The dichroic mirror and delay stage enable adjustment of the relative timing between the native 1070 nm and doubled 2140 nm components of the supercontinuum so that they are temporally coincident. An optical band-pass filter centered at 1070 nm selects the supercontinuum components required for self-referencing, shown in Fig. 3a, and impinging the filtered light on a photodetector reveals the carrier-envelope offset frequency of the EOM comb, shown in Fig. 3b. Note that downsampling introduces an ambiguity in the offset frequency due to the increased density of comb modes in the downsampled pulse train; this ambiguity can be removed by measuring the change in measured offset frequency with a change in $f_r = \omega_r/2\pi$ provided by the

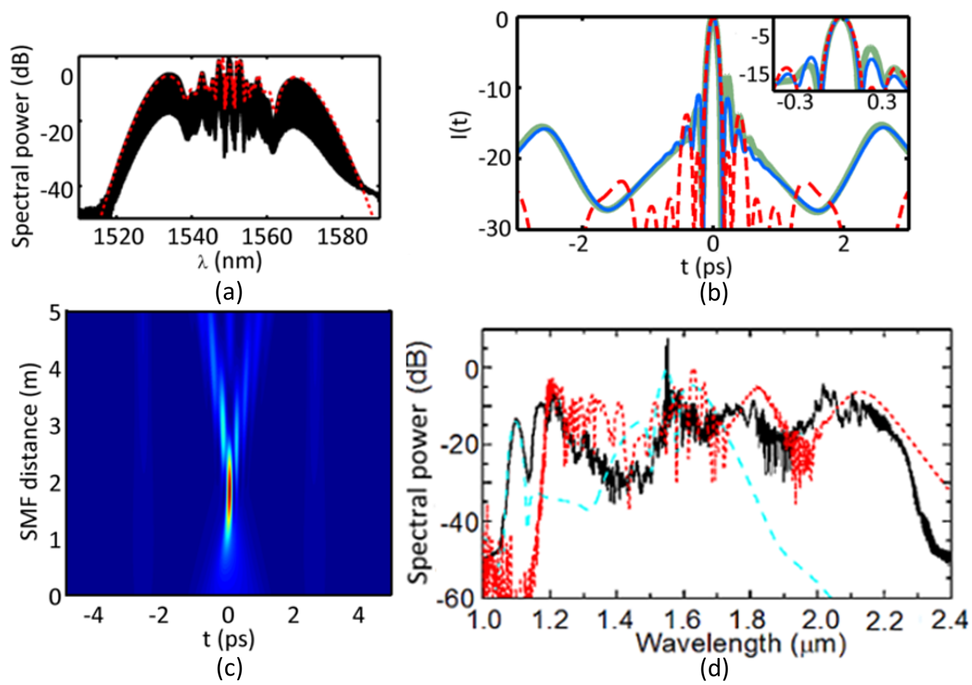

Figure 5.2: **Spectral broadening for generation of an octave-spanning supercontinuum.** (a) Measured optical spectrum after propagation in 100 m of low-normal-dispersion HNLF (black). The spectrum is broadened by self-phase modulation, which imposes a chirp on the pulses. Shown in red is a simulation of the same, conducted as described in the text. (b) Logarithmic-scale plot of the simulated pulse intensity envelopes after temporal recompression in the SLM with 2^{nd}-, 3^{rd}-, and 4^{th}-order dispersion (blue), in an appropriate length of SMF (thick green), to the transform limit (dashed red). (c) Simulated re-compression of the SPM-chirped pulses (red spectrum in panel (a)) in SMF. (d) Measured optical spectrum of the octave-spanning supercontinuum generated by the EOM comb system (black), plotted along with simulated spectra calculated as described in the text to investigate the effects of the 30 cm, highly-dispersive piece of HNLF (long-dashed teal) and the 7.7 m, lower-dispersion piece of HNLF (short-dashed red).

synthesizer driving the modulators.

5.3 Noise in EOM Combs

An important difference between the EOM comb scheme and other approaches for generation of frequency combs is that the repetition rate is derived from a microwave source and is multiplied directly by a factor N to yield the optical frequency of the frequency-comb mode with number N referenced to the seed laser (where $N = 0$). Therefore, the contribution to the optical frequency noise of mode number N from the microwave source scales with the mode number N, and the contribution to the power spectrum of frequency noise scales as N^2. This presents a challenge in the

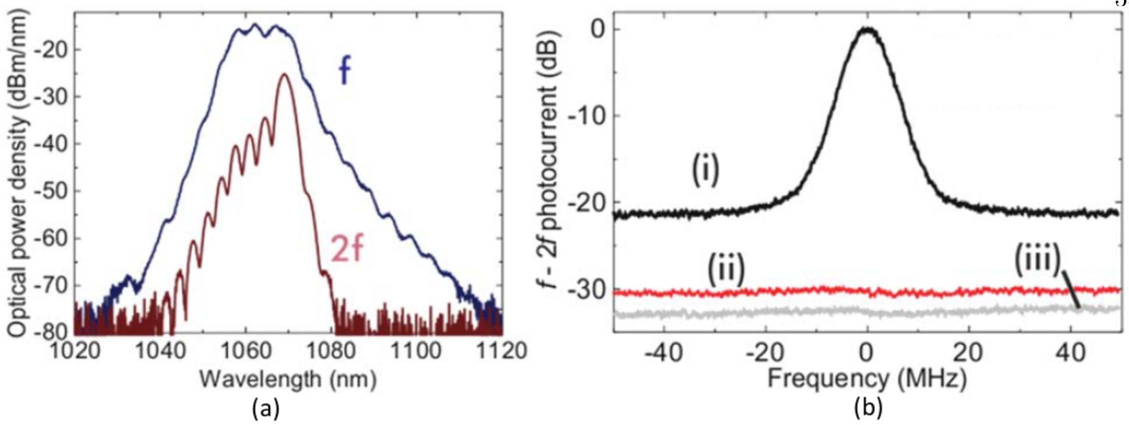

Figure 5.3: **Self-referencing of an EOM comb.** (a) Spectral components used for $f-2f$ self-referencing after passing through a 1070-nm optical bandpass filter: native supercontinuum light (blue) and frequency-doubled 2140-nm supercontinuum light (red) ARE THESE LABELED CORRECTLY. (b) Photodetected carrier-envelope offset frequency signal (black), along with a measurement of the intensity noise of the pulse train obtained by blocking one of the paths (red) and the photodetector noise floor (grey). The intensity-noise measurement highlights the presence of a broad background noise floor on the f_0 signal that must be the result of frequency fluctuations because it is not present when photodetecting either path alone.

generation of coherent supercontinuum light, where the modes relevant for $f-2f$ self-referencing are far separated from the seed laser and N is large. The factor by which the noise on the modulation tone f_r is multiplied to determine its contribution to the noise on the measured carrier-envelope offset frequency is the ratio between the comb's carrier frequency (the frequency of the seed laser) and the repetition rate: $N = f_c/f_r$ =19340 for the 10 GHz comb discussed above (where f_c =193.4 THz for a 1550 nm seed laser). This contribution is shown in Fig. 3a, along with the contribution from the CW seed laser. The noise on f_r results from technical noise on the synthesizer tone at low Fourier frequencies and approaches a white Johnson-Nyquist (thermal) phase-noise floor of -177 dBm/Hz at high Fourier frequencies. Noise in each of these regimes impacts the photodetected f_0 signal: low-frequency noise contributes to the linewidth of the comb modes and therefore the f_0 signal, while high-frequency noise contributes to a frequency-noise floor on the photodetected signal[68]. As discussed in Ref. [66], unmitigated multiplication of this noise floor by the factor N^2 =19340^2 leads to a supercontinuum with optical frequency fluctuations that are large enough to prevent detection and measurement of f_0.

To address this problem and enable $f - 2f$ self-referencing of our comb, we pass the comb through a Fabry-Perot filter cavity whose free-spectral range is actively stabilized to the comb's mode spacing. The filter cavity's Lorentzian transfer function reduces the optical frequency fluctuations of the comb modes at high frequency – these fluctuations are averaged over the photon lifetime of the cavity. This enables generation of a supercontinuum with resolvable modes that is suitable for $f - 2f$ self-referencing and measurement of f_0.

The filter cavity used for this 10 GHz comb has a 7.5 MHz linewidth; equivalently, it has finesse of F ~1333. The effect of passing the comb through the cavity is demonstrated concretely in Fig. 3b, where we compare the lineshape of a heterodyne beat between the supercontinuum and a CW laser with 1319 nm wavelength with and without the filter cavity in place. The signal-to-noise ratios for the beat with and without the filter cavity are 40 dB and 17 dB, respectively.

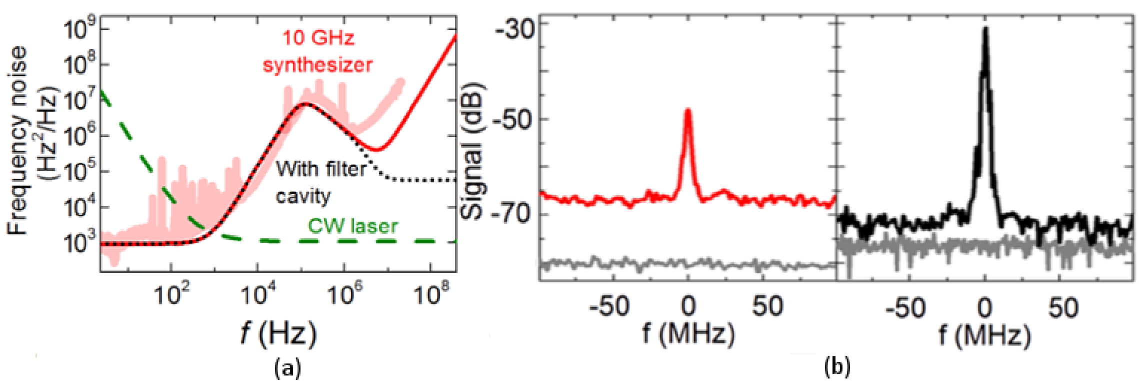

Figure 5.4: **Investigation of the noise properties of the EOM comb.** (a) Contributions to the fluctuation spectrum of the carrier-envelope offset frequency: model of the input seed laser (dashed green), model of the 10 GHz synthesizer multipled by 19430^2 without the filter cavity (solid red, experimental data thick red), and synthesizer multiplied by 19340^2 and the Lorentzian filter-cavity transfer function (dotted black). (b) Comparison of the detected beats between the supercontinuum and a 1519 nm-wavelength CW laser without (red, left) and with (black, right) the Fabry-Perot filter cavity. The level of intensity noise on the supercontinuum, measured by removing the 1319 nm CW laser, is shown by the lower gray trace in each plot. Signal-to-noise ratios for the beat are 17 dB without and 40 dB with the filter cavity.

We also explore the effect of low-frequency fluctuations in the modulation tone f_r by changing the source of this tone. The f_0 signal shown in Fig. **??**b is acquired with a tunable commercial synthesizer providing f_r. In Fig. **??** we show the detected f_0 signal with a dielectric-resonator oscillator and a sapphire oscillator providing f_r; these sources have less low-frequency noise, and the effect of this lower noise is readily apparent in the reduced linewidth of the f_0 signal.

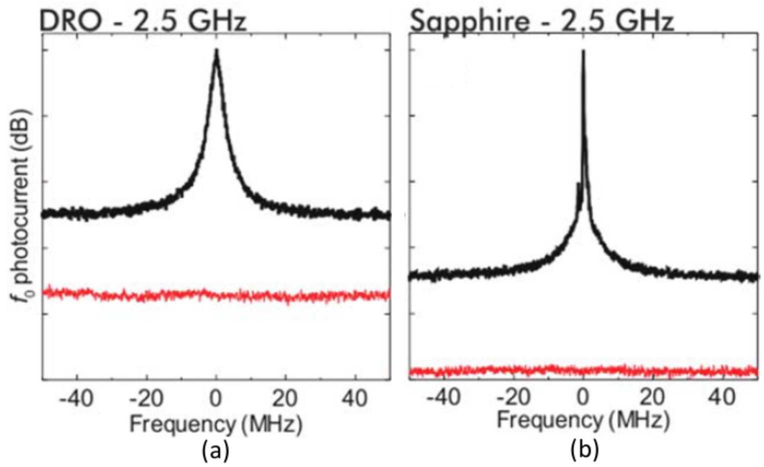

Figure 5.5: **Photodetected carrier-envelope-offset frequency signal with different sources for f_r.** (a) The f_0 beat resulting from a dieletric-resonator oscillator source for the modulation frequency. (b) Ibid with a sapphire oscillator as the source for f_r, which has lower noise than both the tunable commerical synthesizer and the DRO. The reduction in linewidth associated with the change in the source for f_r shows the effect of low-Fourier-frequency noise of f_r on the frequency-noise characteristics of the EOM comb.

Chapter 6

Pulse Picking

This chapter presents a discussion of a technique for repetition-rate reduction of optical pulse trains. While high pulse train repetition rates are appealing for some applications, they are not always appropriate. For example, spectral resolution in spectroscopy applications is sacrificed in a comb with a large mode spacing, and a high repetition rate makes nonlinear optics less efficient at a given average power. This can present a barrier to the generation of octave-spanning spectra for $f - 2f$ self-referencing (see App. ??). On the other hand, in general the size of the comb package sets the scale for the round-trip time, meaning that low-SWAP combs generally have inherently high repetition rate. Therefore, to increase the flexibility of low-SWAP and high-repetition-rate comb systems in applications, a method for reducing the repetition rate of a pulse train will be useful.

Here I present an investigation of a method for repetition-rate reduction, or downsampling, in which an electro-optic gate realized by an RF-driven Mach-Zehnder interferometer periodically transmits an incoming pulse at a frequency lower than the input repetition rate. The basic principle is illustrated in Fig. 6.1. Downsampling via pulse gating, also referred to as 'pulse picking' in the literature, has been used extensively in the context of high-field, phase-sensitive ultrafast optics for the generation of energetic, carrier-envelope-phase-stabilized ultrashort pulses[69, 70]. In this application, a comb with initial repetition rate in the ~100 MHz range that has already been stabilized is pulse-picked to a repetition rate on the order of 1-100 kilohertz. Concerns in this application center around control and preservation of the carrier-envelope phase in the pulse-picking and amplification process[71, 72]. In contrast, the focus here is on downsampling within the context of optical metrology with frequency combs, and we are concerned with downsampling's effect on the optical phase noise, the pulse-to-pulse energy fluctuations, and the carrier-envelope offset frequency of the frequency comb. In particular, it is important that the downsampled pulse train is suitable for $f - 2f$ self-referencing.

Sec.6.1 presents a proof-of-principle experiment in which a 250 MHz pulse train is downsampled to 25 MHz, and then spectrally broadened and self-referenced. A mathematical model of downsampling is presented in Sec. 6.2, and this model informs the discussion of downsampling's effect on the pulse train's noise properties presented in Sec. 6.3 and Sec. 6.4. In Sec. 6.4.1 I discuss some practical considerations in applications of the technique, including the effect of imperfections in the gating process such as incomplete extinction of rejected pulses.

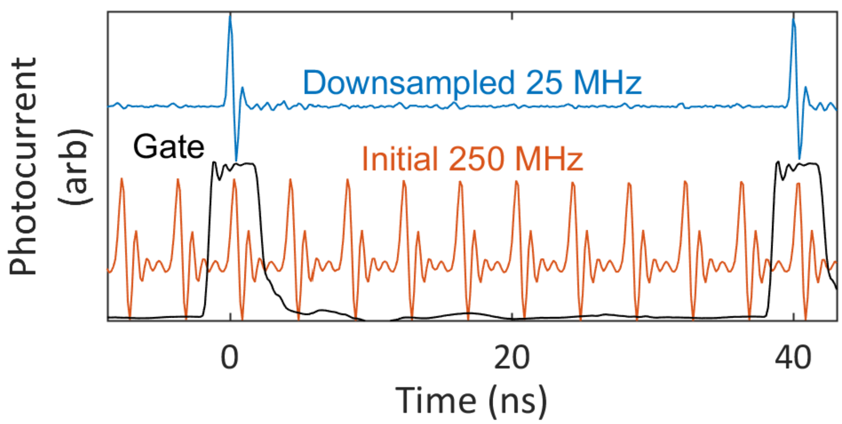

Figure 6.1: **An illustration of downsampling.** Orange: A photodetected 250 MHz pulse train. Blue: A photodetected 25 MHz pulse train obtained by downsampling the 250 MHz pulse train by a factor of $N = 1/10$. Black: Oscilloscope trace showing the voltage sent to the RF port of a Mach-Zehnder intensity modulator to selectively transmit a subset of the incoming pulses. With the intensity modulator biased for zero transmission, the voltage trace is indicative of the transmission.

6.1 Proof-of-Concept Experiment

Here I present a proof-of-concept experiment in which a 250 MHz comb is downsampled and self-referenced.

The application of downsampling to the detection of the carrier-envelope offset frequency of a 250 MHz comb is shown in Fig. 6.2. Our pulse gating scheme, shown in Fig. 6.2a, employs a Mach-

Zehnder (MZ) electro-optic intensity modulator driven by 25 MHz rectangular electronic gating pulses with 80 ps transitions and 3.5 ns duration. The electronic pulse generator and the repetition rate of the input 250 MHz comb are both referenced to a hydrogen maser to maintain synchronization. The DC bias of the intensity modulator is set for maximum extinction outside the electronic gate, whose amplitude is approximately matched to V_π of the EOM. This downsampling scheme results in a stable 25 MHz optical pulse train with >12 dB contrast (Fig. 6.1b). This contrast is adequate for this experiment, but could be improved by cascading modulators with higher extinction ratios. The average power of the 250 MHz pulse train is reduced from 30 mW to 400 μW by the pulse gating process and the insertion loss of the optical components. The pulse train is amplified to 35 mW by use of a normal-dispersion erbium-doped fiber amplifier, which provides some spectral broadening and temporal pulse compression 22. An octave-spanning supercontinuum is obtained by launching the amplified, <100 fs, $\sim$1 nJ pulses into 20 cm of highly nonlinear fiber (HNLF)[73]; the resulting spectrum is shown in Fig. 6.2c. For comparison, we also present the supercontinuum generated by the 250 MHz comb with the EOM set for constant maximum transmission under otherwise identical conditions. The 250 MHz comb is amplified by the same EDFA to an average power of 85 mW, corresponding to 340 pJ pulse energy, before it enters the HNLF.

To detect f_0, the octave-spanning supercontinuum shown in Fig. 6.2b is sent into a free-space $f - 2f$ interferometer consisting of a half-wave plate and a periodically poled lithium niobate (PPLN) crystal quasi-phase-matched for second-harmonic generation at 1980 nm. The generated 990 nm light is shown in 6.2b. A 10 nm band-pass filter at 990 nm selects this second harmonic and the co-linear supercontinuum at 990 nm, which are then photodetected to observe f_0 with 30 dB signal-to-noise ratio, shown in Fig. 6.2c. Fig. 6.2d shows a 2000 s record of f_0 for the downsampled comb.

6.2 Mathematical model for downsampling

While Fig. 6.2 presents an absolute frequency measurement of f_0 enabled by downsampling, it does not demonstrate the deterministic connection between the input and downsampled combs

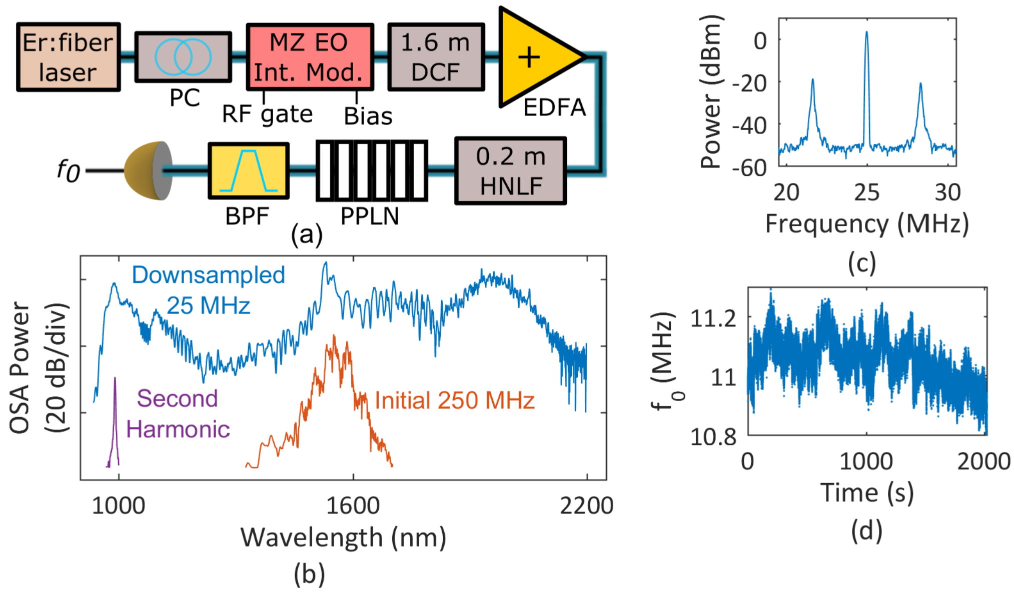

Figure 6.2: **Demonstration of downsampling for f_0 detection.** (a) Schematic for downsampling a 250 MHz Er:fiber comb and detecting the offset frequency of the resulting 25 MHz pulse train. PC – polarization controller. DCF – dispersion-compensating fiber. EDFA – erbium-doped fiber amplifier. HNLF – highly nonlinear fiber. PPLN – periodically-poled lithium niobate. BPF – (optical) band-pass filter.(b) Octave-spanning supercontinuum generated by downsampling (top, blue), second harmonic generated for f0 detection (purple), and for comparison the supercontinuum generated by the same apparatus without downsampling (orange). (c) Detected repetition rate and f_0 beat at 100 kHz RBW; signal-to-noise ratio of f_0 is 30 dB. e) Counted frequency of the detected free-running offset beat. Data is taken for 2000 s at 10 ms gate time. The offset frequency of the 250 MHz commercial comb was adjusted between measurements shown in Figs. 6.2c and 6.2d to simplify electronic processing.

that is essential for applications. To understand this relationship, I present first a simple model of downsampling, and then experimental tests of its conclusions.

The downsampled pulse train's electric field is modeled as the product of the incoming comb's field and a time-varying amplitude modulation. For an incoming optical frequency comb with repetition rate f_r, complex single-pulse field $A(t)$ that is localized near $t = 0$, and pulse-to-pulse carrier-envelope phase shift ϕ, pulse gating by a train of rectangular pulses of length t_g and arrival rate f_g yields a downsampled comb with field

$$a(t) = \left[\Sigma_n A(t - n/f_r)e^{in\phi}\right] \times \left[\Sigma_m \mathrm{Rect}\left((t - m/f_g)/t_g\right)\right] \tag{6.1}$$

where $\mathrm{Rect}(x)$ is the rectangle function, taking the value 1 for $-1/2 \leq x \leq 1/2$ and 0 elsewhere. Indices n and m count the pulse number of the incoming pulse train and the electronic gate respectively. The optical spectrum of the downsampled pulse train $a(t)$, calculated via the convolution theorem for the Fourier transform, is:

$$\mathcal{F}\{a\}(f) \sim 4\pi f_r \Sigma_{nm} \frac{1}{m} \mathcal{F}\{A\}(f_0 + nf_r) \times \sin(\pi m t_g f_g)\delta(f - f_0 - nf_r - mf_g) \tag{6.2}$$

where $f_0 = (f_r \cdot \phi/2\pi$ is the carrier-envelope offset frequency of the incoming comb and δ is the Dirac delta function. The downsampled pulse train has spectral content at optical modes $f_0 + nf_r$, as well as at intensity modulation sidebands whose frequency offsets mf_g are harmonics of the gating frequency. To avoid the generation of unwanted modulations, pulse gating at an integer sub-harmonic of the incoming repetition rate, $f_g = f_r/N$, is essential. In this case superposition of the intensity modulation components created by pulse gating results in a downsampled frequency comb with a single mode spacing. Moreover, this model predicts that the offset frequency is preserved up to a reduction modulo the comb's new repetition rate.

Notably, for pulse gating at a sub-harmonic of the input comb's repetition rate, timing jitter of the electronic gate that is less than its duration does not contribute to noise on the downsampled comb. By modelling jitter as gate-to-gate arrival-time delays Δt_m, it can be shown that the downsampled comb's amplitude $a(t)$ and spectrum $F\{a\}(f)$ do not deviate from Eqn. 6.1 provided that: 1) The jitter is a sufficiently small $|\Delta t_m| < t_g/2$, i.e., that the optical and electronic pulses are always substantially overlapped, and 2) That the optical pulses are substantially shorter than the electrical pulses, which is true for most systems. Thus, in general we expect that the carrier-envelope offset frequency of the incoming comb is preserved by downsampling even with jitter on the gate signal.

6.3 Experimental investigation of the effect of downsampling on the pulse train's noise properties

We supplement the mathematical model presented above with an experimental investigation of the effects of downsampling on the noise properties of the pulse train. First we consider the effects of technical limitations to ideal downsampling, and then we discuss fundamental effects associated with aliasing of high-Fourier-frequency optical noise and shot noise.

We measure the phase-noise spectrum of the downsampled comb's repetition rate at different points in our apparatus, as shown in Fig. 6.3a. We also plot the phase noise of the 250 MHz comb, which has been shifted by $-10\log_{10}(N^2) = -20$ dB to facilitate comparison[74], and the phase noise of the electronic gate. The downsampled frequency comb's phase-noise spectrum matches that of the 250 MHz comb except for a small increase at $\sim$3 kHz, likely corresponding to the corner in the gate generator's phase noise at the same frequency. The phase noise of the high- and low-frequency ends of the supercontinuum similarly matches the 250 MHz comb below 1 kHz. The higher phase noise in the supercontinuum beyond 1 kHz is likely due to noise generation processes in the HNLF, such as the conversion of amplitude fluctuations on input pulses to timing jitter in the supercontinuum[64].

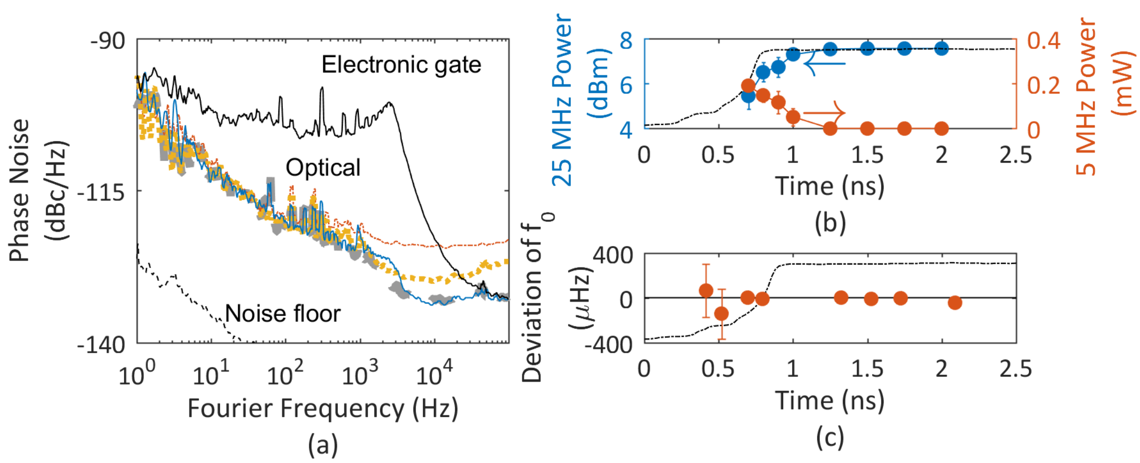

Figure 6.3: **Experimental investigation of noise introduced by downsampling.** (a) Measured repetition-rate phase noise of spectral components of the supercontinuum, selected by a 990±5 nm band-pass filter (dot-dashed orange), 1650 nm long pass filter (dotted yellow), and the entire downsampled 25 MHz frequency comb measured immediately before the EDFA (solid blue), the 250 MHz comb (large-dashed gray, shifted by $20\log(1/10) = -20$ dB. Also shown is the phase noise of the electronic gate generator (top, solid black). (b) Amplitude of the downsampled pulse-train modulation due to 250 ps jitter at 5 MHz rate. The position of a data point on the x-axis indicates its mean position within the gate, shown in dashed black. Measurement uncertainties arise due to a latency between the optical trigger and the start of the electronic gating signal which varies on the order of 50 ps. (c) Deviation of the carrier-envelope offset frequency of the downsampled comb from the 250 MHz comb's offset frequency as a function of the alignment of optical pulses within the gate.

The timing jitter of our gating pulse train is between 5 ps (obtained by integrating the phase noise plotted in Fig. 6.3 to 100 kHz) and 10 ps (extrapolating constant phase noise to the 12.5 MHz Nyquist frequency and integrating). These jitter values are small relative to the 4 ns repetition period of the incoming optical pulse train. As the repetition rate of the incoming optical pulse train increases to >10 GHz, the gate duration must correspondingly decrease for single-pulse gating, and timing jitter on the gate may become a significant fraction of the gate duration. To explore the effects of timing jitter larger than our pulse generator's inherent 5 to 10 ps, we impose excess jitter on the gating signal. We modulate the relative timing between the gating signal and the incoming optical pulse train at a frequency of 5 MHz with an amplitude of 250 ps. The effect of this jitter is manifest in the microwave power of the gated comb as 5 MHz intensity-modulation sidebands whose amplitude depends on the position of the optical pulses within the gate, as shown in Fig. 6.3b. Pulses with a mean position within 250 ps of the gate edge are substantially modulated by the 5 MHz gate-delay signal. This agrees with the prediction of a sharp threshold on the acceptable level of timing jitter on the gate.

It is essential to establish that the comb's carrier-envelope offset frequency is preserved in the downsampling process. To do this, we perform a frequency comparison of the 25 MHz downsampled comb and a separate output of the 250 MHz comb. This 250 MHz output is intensity modulated so that a measurement of the nonzero optical heterodyne beat frequency between an intensity modulation sideband and a pulse-gating sideband of the downsampled comb reveals the relative frequency offset of the two combs. Figure 6.3c shows the null frequency shift between the 25 MHz and 250 MHz combs, which we have characterized for different alignments of the optical pulse within the gate. At the level of several microhertz, better than 10^{-18} relative to the 200 THz optical carrier frequency, we observe no frequency shift between the 250 MHz comb and the downsampled 25 MHz comb when the gate is properly aligned. This confirms the utility of downsampling for measurement of a high-repetition-rate comb's offset frequency for subsequent use of the comb in, for example, a spectroscopy experiment requiring high power per comb mode and high frequency precision.

6.4 Effects of ideal downsampling on a pulse train's noise properties

In addition to the conversion of electronic technical noise to optical noise on the downsampled pulse train, there exists a further mechanism by which downsampling can change the measured amplitude noise properties of the pulse train. Even ideal downsampling, free of electronic noise, leads to an increase in the measured power spectral density (PSD) of optical pulse energy fluctuations (PEF) when technical pulse energy noise is present. This is due to aliasing of components of the PSD of pulse energy fluctuations at frequencies above the Nyquist frequency, $f_r/2$, when the Nyquist frequency is reduced by downsampling. Assuming random fluctuations from pulse to pulse, downsampling does not change the RMS fractional pulse energy fluctuation σ_{PEF}, whose square is equal to the frequency integral of the PSD of pulse energy fluctuations $S_{PEF}(f)$:

$$\sigma_{PEF}^2 = \int_0^{f_r/2} df S_{PEF}(f). \tag{6.3}$$

—

Because the Nyquist frequency $f_r/2$ defines the upper limit for integration of S_{PEF}, in order for σ_{PEF} to be preserved $S_{PEF}(f)$ must increase when the Nyquist frequency is reduced. For example, in the simple case of white technical noise on the pulse energies with density S_o, we have

$$\sigma_{PEF}^2 = \int_0^{f_r/2} df S_o = \int_0^{f_r/2N} df S^{'} \tag{6.4}$$

which shows that downsampling must increase the measured PSD of white technical noise from S_o to $S^{'} = NS_o$, assuming there are no spectral correlations. However, this simple multiplicative increase is restricted to the case of white technical noise. In general, the PSD of pulse energy fluctuations of the new pulse train is determined from the original PSD through the usual method of modeling aliasing of a signal: a new Fourier frequency for each component of the original PSD is obtained by reducing the original Fourier frequency by a multiple of $-f_r/N$ so that it lies between $-fr/2N$ and $f_r/2N$ and taking its absolute value. The new PSD is then determined by taking the quadrature sum of the PSD components at the same aliased Fourier frequency. This phenomenon is derived mathematically and demonstrated experimentally in Ref. [71], where the analysis of carrier-envelope phase noise applies equally well to pulse energy fluctuations.

In contrast with the increase in the PSD of pulse energy fluctuations arising from coincidence of the optical pulse with the edge of the electrical gate, which increases σ_{PEF}, the aliasing mechanism described above preserves σ_{PEF}. An important consequence of this is that while technical noise can lead to supercontinuum decoherence in external nonlinear spectral broadening, aliasing does not, because it is σ_{PEF} which determines the degree of supercontinuum decoherence. Thus the aliasing mechanism impedes $f-2f$ self-referencing only by reducing the available signal-to-noise ratio of an f_0 signal in a straightforward linear fashion.

In practice, the relevance of the aliasing of the PSD of pulse energy fluctuations is determined by the presence of technical noise on the pulse energies at high Fourier frequency $f > f_r/2N$. For sufficiently small downsampling factors (e.g. $f_r/2N \leq\sim 50MHz$) and depending on the comb source, it is possible that the only source of intensity noise at frequencies above $f_r/2N$ is shot noise. Shot noise results in a maximal (shot-noise-limited) signal-to-noise (SNR) ratio of an optical heterodyne beat with a local oscillator laser which is reduced by N^2 (in electrical power units) as the average power of the pulse train is reduced by downsampling by a factor of N. In contrast, in the case of detection of a carrier-envelope-offset beat with fixed optical detection bandwidth, the shot-noise-limited SNR is preserved in downsampling. One way to understand these results is to model the shot noise at a given Fourier frequency as the incoherent sum of optical heterodyne beats between each optical comb mode and the uncorrelated vacuum fluctuations at the appropriate optical frequency25,26, and to take into account the fact that during downsampling the optical power of each comb mode is reduced by N^2, with the first factor of N coming from reduction of the total optical power and the second factor of N due to the increase in the spectral density of comb modes.

We experimentally investigate the impact of downsampling on the PSD of pulse energy fluctuations by measuring noise on three photodetected optical signals: a shot-noise-limited telecom-band CW laser, a 10 GHz pulse train generated by passing this laser through cascaded optical phase and intensity modulators (see Chapter **??**, [75]) and then a low-noise EDFA, and this pulse train after downsampling by a factor of four to 2.5 GHz repetition rate with no additional amplification after downsampling. Shown in Figure 6.4 are curves for each signal of the fluctuations $\sqrt{S_I(f = 50\,\mathrm{MHz})}$ in the detected photocurrent at a Fourier frequency of 50 MHz versus the total time-averaged detected photocurrent $\langle I \rangle$ from the optical signal. To measure the scaling of noise with optical power, these curves are generated by beginning with an optical signal which yields more than 800 μA of detected photocurrent and attenuating this signal before photodetection. The data indicate that both the pulse-generation process and the downsampling process contribute some amount of technical noise at 50 MHz Fourier frequency to the photocurrent, because the measured curves are well-modeled by a quadrature sum of a shot-noise contribution and a technical noise contribution. The contributions of these two types of noise can be determined because they scale differently with the photodetected power: shot noise obeys the relationship $\sqrt{S_I(f = 50\,\mathrm{MHz})} = \sqrt{2e\langle I \rangle}$, $\langle I \rangle$ denoting the time-averaged photocurrent, while the technical-noise contribution arises from fluctuations in the expected photocurrent $I(t)$ and scales linearly with the detected photocurrent. We observe that downsampling by a factor of four leads to a multiplication of the amplitude of the technical noise by a factor of $\sim$1.7 on the optical signal relative to the carrier, which due to finite noise bandwidth is somewhat less than the factor of two (four, in electrical power units) which would be expected for ideal downsampling by a factor of four in the presence of white technical noise. These results further demonstrate that, properly implemented, downsampling does not magnify noise on the pulse train to a degree which is prohibitive for applications.

6.4.1 Model for the effect of incomplete extinction of rejected pulses and amplification of a downsampled pulse train

To this point, we have considered effects of downsampling assuming that extinction of the rejected pulses is complete, but in a practical application this is not necessarily the case. The modulators used for pulse extinction may transmit a substantial amount of energy from the rejected pulses—for example, one commercial manufacturer specifies 25 dB extinction ratio, this number vary in practice. Additionally, the electronic gating signal may not have sufficient bandwidth to completely switch from transmission to extinction within the repetition period of the incoming pulse train, and initial extinction can be followed by some transmission caused by ringing in the gating signal. Bandwidth limitations will be increasingly likely as the repetition rates of frequency

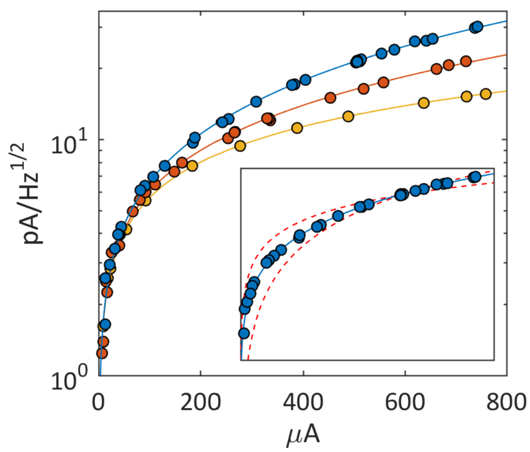

Figure 6.4: **Effect of downsampling on photocurrent fluctuations.** Fluctuations at 50 MHz Fourier frequency in the detected photocurrent as a function of the time-averaged photocurrent in three cases: CW laser at the shot-noise limit (lowest, yellow), 10 GHz pulse train (middle, red), and 2.5 GHz down-sampled pulse train (highest, blue). Dots show measured data and curves show fits to the data. The fit for the shot-noise-limited laser has a single free parameter, which is a scaling factor of order 1 due to frequency dependence of the photo-detector's trans-impedance gain. The fits for the pulse trains have a scaling factor in common, and have as an additional parameter the amplitude of the technical noise on the pulse train. This is -153.9 dBc/Hz for the 10 GHz pulse train and increases by a factor of ∼1.72 to -149.3 dBc/Hz for the 2.5 GHz downsampled pulse train. Inset: Optimized fits (dashed red) to the experimental data for the downsampled 2.5 GHz pulse train using only shot-noise or linear technical noise scaling, demonstrating that both noise processes are important for explaining the data.

combs increase, placing more demanding requirements on gating electronics. Incomplete extinction will add modulations to the optical spectrum and will raise the total power of the downsampled pulse train while keeping the energy of the fully-transmitted pulses fixed. This will require higher average power to achieve a given target pulse energy.

The effects of incomplete extinction of rejected pulses are exacerbated if the incomplete extinction does not happen in a deterministic and repetitive fashion; this could occur, for example, if intermediate pulses fall near the edge of the gate in the presence of relative timing jitter between the optical and electronic pulse trains; or if the extinction ratio fluctuates in time. Interestingly, if the downsampled pulse train is subsequently amplified and spectrally broadened, the impact of incomplete extinction depends on whether the optical amplifier used operates in the linear regime or in the saturated regime.

As an example, we consider the case where each fully transmitted pulse is preceded and followed by partially-extinguished pulses whose amplitudes fluctuate for each period of the downsampled pulse train. This fluctuation could occur because the pulses lie on the edge of the electronic gate and there is relative timing jitter between the optical pulse train and the gating signal. It is true that these fluctuations will lead to decoherence during nonlinear spectral broadening. However, the coherence is degraded by this mechanism only within the bandwidth that is achieved by the broadened, partially-extinguished pulses. In efficient $f-2f$ interferometry only the fully-transmitted pulses should reach an octave in bandwidth. Therefore, this mechanism of supercontinuum decoherence is not a problem in $f-2f$ interferometry in general, unless there is coupling between the amplitudes of the amplified partially-extinguished pulses and the amplified fully transmitted pulses. This coupling can arise, for example, through amplification in the saturation regime, which then leads to decoherence across the full bandwidth of the supercontinuum.

To illustrate this point, we have performed numerical simulations of the spectral broadening of a 100 GHz train of 100 fs pulses which has been downsampled to 10 GHz and then amplified. We use an adaptive[76] split-step Fourier method[77] to simulate spectral broadening in 30 cm of HNLF according to the generalized nonlinear Schrodinger equation[15] (see Appendix **??**. In the simulation each fully-transmitted pulse, amplified to 1 nJ, is preceded and followed by partially-extinguished pulses with normally distributed and uncorrelated energies with mean of 0.3 nJ and standard deviation of 0.225 nJ. This models the effect of adjacent pulses which coincide with the edge of the gate. We simulate amplification in two regimes: saturation is simulated using a fixed-energy method wherein the pulse energies in each three-pulse burst are re-scaled by a common factor so that the total energy is 1.6 nJ; linear amplification is simulated using a fixed-gain model, which involves no such rescaling of pulses. Numerically, we simulate the spectral broadening of each pulse individually, which is acceptable because terms in the generalized non-linear Schrodinger equation operate only locally or, in the case of the Raman term, on the timescale of several femtoseconds, while the separation between the pulses in each burst is 10 ps (the inverse of the initial 100 GHz repetition rate). We have verified that during simulated time-evolution each broadened pulse remains well-centered in its 5 ps simulation window.

Results of this study are shown in Figure 6.5. Figure 6.5a depicts a three-pulse burst before and after propagation in HNLF. In Figure 6.5b we show spectra corresponding to spectral broadening of this three-pulse burst, as well as plots of the spectral coherence averaged over many simulations. The first-order spectral coherence $g_{12}^{(1)}(\lambda)$ is defined as:

$$\left|g_{12}^{(1)}(\lambda)\right| = \left|\frac{\langle E_1^*(\lambda)E_2(\lambda)\rangle}{\sqrt{\langle|E_1(\lambda)|^2\rangle\langle|E_2(\lambda)|^2\rangle}}\right| = \left|\frac{\langle E_1^*(\lambda)E_2(\lambda)\rangle}{\langle|E(\lambda)|^2\rangle}\right|. \tag{6.5}$$

Curves are plotted for the fixed-gain and fixed-energy cases, as well as for the case with ideal downsampling (no partially-extinguished pulses) and only shot-noise on the pulse train. The averages in the formula above are over 1000 instantiations of the pair E_1 and E_2, for a total of 2000 broadened spectra for each pulse within the burst of three. In both the fixed-gain and fixed-energy cases the coherence is poor in the center of the spectrum, but in the fixed-gain case, which models amplification in the linear regime, the coherence is preserved in the high- and low-frequency ends of the spectrum where it is needed for self-referencing.

6.4.2 Further remarks on the application of downsampling

Downsampling via pulse gating is a promising tool to manipulate high-repetition-rate frequency combs from low size, weight, and power packages and to aid in the detection of their offset frequencies. In our experiments downsampling enabled detection of f_0 at a signal-to-noise ratio sufficient for measurement and stabilization, which otherwise would have required significantly higher average power. The effects of the electronic timing jitter of the gate signal are negligible so long as incoming optical pulses do not arrive coincidentally with the edge of the gate; when they do, timing jitter induces amplitude noise on the transmitted pulses. This results in an increase in RMS optical pulse energy fluctuations σ_{PEF}. Independently, the PSD of pulse energy fluctuations may be increased by aliasing of technical noise and by shot noise, depending on the relative magnitudes of these two types of noise. Each of these sources of signal-to-noise-ratio degradation has the potential to interfere with detection of f_0. This investigation of these challenges will facilitate application of the technique in high-repetition-rate frequency comb systems. Importantly, our experiments demonstrated that

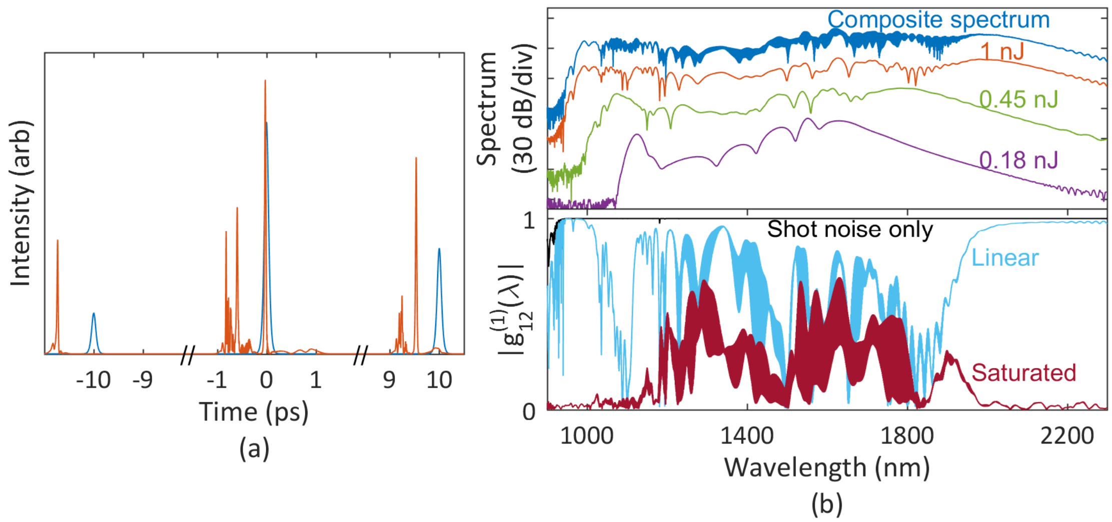

Figure 6.5: **Investigation of incomplete pulse extinction and amplification.** Investigation of incomplete pulse extinction and amplification. (a) A burst consisting of a fully-transmitted 1 nJ, 100 fs pulse and 100 fs partially-transmitted adjacent pulses with energies of 0.18 nJ and 0.45 nJ. Blue indicates initial sech^2 pulses, and orange indicates the intensity after propagation through 30 cm HNLF. Note that the x-axis has been broken. (b) Top panel: optical spectra corresponding to the pulses shown in orange in (a), showing the composite spectrum of the three pulses (top, blue) and the spectra of the 1 nJ central pulse (second, orange), the 0.45 nJ adjacent pulse (third, green), and the 0.18 nJ adjacent pulse (bottom, purple). Bottom panel: Calculated spectral coherence averaged over 2000 simulations for the case of shot-noise only (top, black) and for the case of fluctuating amplitudes of the first and last pulses as described in the text, after simulated amplification in a linear-regime optical amplifier (second, teal), and a saturated optical amplifier (bottom, maroon). For the case of linear-regime operation, high spectral coherence is preserved in the extreme ends of the supercontinuum even as it is lost in the center, in contrast with the complete loss of coherence after amplification in saturation.

downsampling does not add a significant amount of noise to the frequency components of the pulse train, and in a separate experiment the technique has recently been used successfully to detect the carrier-envelope offset frequency of a 10 GHz comb by downsampling by a factor of four[66].

To employ downsampling as demonstrated here with repetition rates >10 GHz will require electronic gates with duration ≤100 ps. Technology to downsample with gates as short as 20 ps is commercially available, while 100 Gb/s integrated circuits and 25 GHz demultiplexing have been demonstrated[78, 79]. Barring the use of such state-of-the-art electronics, pulse gates of duration longer than the incoming optical pulse train's repetition period can be employed. This will be technically easier to achieve, but will result in additional modulations on the spectrum of the downsampled pulse train.

The ambiguity of the input comb's offset frequency as a result of the reduction of the offset frequency modulo the new repetition rate makes downsampling most suitable for applications where the ambiguity can be removed by some other method. Two such applications are frequency comb calibration of astronomical spectrographs, where measurement of the wavelength of a comb mode can remove the ambiguity, and microresonator-based frequency combs, where the uncertainty in the offset frequency is determined by the frequency stability of the pump laser and can be much less than the repetition rate of the downsampled comb.

References

[1] T. Udem, R Holzwarth, and T. W. Hänsch. Optical frequency metrology. *Nature*, 416 (6877), **2002**, 233–237. DOI: `10.1038/416233a` (cited on page 1).

[2] J. L. Hall. Nobel lecture: Defining and measuring optical frequencies. *Reviews of Modern Physics*, 78 (4), **2006**, 1279–1295. DOI: `10.1103/RevModPhys.78.1279` (cited on page 1).

[3] T. W. Hänsch. Nobel lecture: Passion for precision. *Reviews of Modern Physics*, 78 (4), **2006**, 1297–1309. DOI: `10.1103/RevModPhys.78.1297` (cited on page 1).

[4] J. K. Ranka, R. S. Windeler, and A. J. Stentz. Visible continuum generation in air–silica microstructure optical fibers with anomalous dispersion at 800 nm. *Optics Letters*, 25 (1), **2000**, 25. DOI: `10.1364/OL.25.000025` (cited on page 1).

[5] T. Steinmetz, T. Wilken, C. Araujo-Hauck, R. Holzwarth, T. W. Hänsch, L. Pasquini, A. Manescau, S. D'Odorico, M. T. Murphy, T. Kentischer, W. Schmidt, and T. Udem. Laser frequency combs for astronomical observations. *Science*, 321 (5894), **2008**, 1335–7. DOI: `10.1126/science.1161030` (cited on page 1).

[6] D. T. Spencer, T. Drake, T. C. Briles, J. Stone, L. C. Sinclair, C. Fredrick, Q. Li, D. Westly, B. R. Ilic, A. Bluestone, N. Volet, T. Komljenovic, L. Chang, S. H. Lee, D. Y. Oh, T. J. Kippenberg, E. Norberg, L. Theogarajan, M.-g. Suh, K. Y. Yang, H. P. Martin, K. Vahala, N. R. Newbury, K. Srinivasan, J. E. Bowers, S. A. Diddams, and S. B. Papp. An optical-frequency synthesizer using integrated photonics. *Nature*, 557, **2018**, 81–85. DOI: `10.1038/s41586-018-0065-7` (cited on pages 2, 24).

[7] R. W. Boyd. **Nonlinear Optics**. San Diego, CA: Elsevier, 2003 (cited on pages 5, 13).

[8] E. Obrzud, S. Lecomte, and T. Herr. Temporal solitons in microresonators driven by optical pulses. *Nature Photonics*, 11 (August), **2017**, 600–607. DOI: `10.1038/nphoton.2017.140`. arXiv: `1612.08993` (cited on pages 7, 24).

[9] P. Del'Haye, S. A. Diddams, and S. B. Papp. Laser-machined ultra-high-Q microrod resonators for nonlinear optics. *Applied Physics Letters*, 102, **2013**, 221119 (cited on page 9).

[10] A. N. Oraevsky. Whispering-gallery waves. *Quantum Electronics*, 32 (42), **2002**, 377–400. DOI: `10.1070/QE2001v031n05ABEH002205`. arXiv: `arXiv:1011.1669v3` (cited on page 9).

[11] H. A. Haus. **Waves and Fields in Optoelectronics**. Englewood Cliffs: Prentice-Hall, 1984 (cited on page 9).

[12] S. M. Spillane, T. J. Kippenberg, O. J. Painter, and K. J. Vahala. Ideality in a Fiber-Taper-Coupled Microresonator System for Application to Cavity Quantum Electrodynamics. *Physical review letters*, 91 (4), **2003**, 043902. DOI: `10.1103/PhysRevLett.91.043902` (cited on page 11).

[13] V. S. Il'chenko and M. L. Gorodetskii. Thermal nonlinear effects in optical whispering gallery microresonators.pdf. *Laser Physics*, 2 (6), **1992**, 1004–1009 (cited on page 11).

[14] T. Carmon, L. Yang, and K. J. Vahala. Dynamical thermal behavior and thermal self-stability of microcavities. *Optics Express*, 12 (20), **2004**, 4742–4750. URL: `http://www.ncbi.nlm.nih.gov/pubmed/19484026http://www.opticsinfobase.org/oe/abstract.cfm?uri=oe-12-20-4742` (cited on page 11).

[15] G. P. Agrawal. **Nonlinear Fiber Optics**. 4th. Burlington, MA: Elsevier, 2007 (cited on pages 13, 16, 21, 50, 67).

[16] R. del Coso and J. Solis. Relation between nonlinear refractive index and third-order susceptibility in absorbing media. *Journal of the Optical Society of America B*, 21 (3), **2004**, 640. DOI: `10.1364/JOSAB.21.000640` (cited on page 13).

[17] P Del'Haye, A Schliesser, O Arcizet, T Wilken, R Holzwarth, and T. J. Kippenberg. Optical frequency comb generation from a monolithic microresonator. *Nature*, 450 (7173), **2007**, 1214–1217. DOI: `10.1038/nature06401` (cited on page 13).

[18] T. Kippenberg, S. Spillane, and K. Vahala. Kerr-Nonlinearity Optical Parametric Oscillation in an Ultrahigh-Q Toroid Microcavity. *Physical Review Letters*, 93 (8), **2004**, 083904. DOI: `10.1103/PhysRevLett.93.083904` (cited on page 13).

[19] A. A. Savchenkov, A. B. Matsko, D. Strekalov, M. Mohageg, V. S. Ilchenko, and L. Maleki. Low threshold optical oscillations in a whispering gallery mode CaF 2 resonator. *Physical Review Letters*, 93 (24), **2004**, 2–5. DOI: `10.1103/PhysRevLett.93.243905` (cited on page 13).

[20] I. H. Agha, Y. Okawachi, M. A. Foster, J. E. Sharping, and A. L. Gaeta. Four-wave-mixing parametric oscillations in dispersion-compensated high- Q silica microspheres. *Physical Review A - Atomic, Molecular, and Optical Physics*, 76 (4), **2007**, 1–4. DOI: `10.1103/PhysRevA.76.043837` (cited on page 13).

[21] F. Leo, S. Coen, P. Kockaert, S.-P. Gorza, P. Emplit, and M. Haelterman. Temporal cavity solitons in one-dimensional Kerr media as bits in an all-optical buffer. *Nature Photonics*, 4 (7), **2010**, 471–476. DOI: `10.1038/nphoton.2010.120` (cited on page 14).

[22] T. Herr, K. Hartinger, J. Riemensberger, C. Y. Wang, E. Gavartin, R. Holzwarth, M. L. Gorodetsky, and T. J. Kippenberg. Universal formation dynamics and noise of Kerr-frequency combs in microresonators. *Nature Photonics*, 6 (7), **2012**, 480–487. DOI: `10.1038/nphoton.2012.127` (cited on page 14).

[23] Y. K. Chembo and C. R. Menyuk. Spatiotemporal Lugiato-Lefever formalism for Kerr-comb generation in whispering-gallery-mode resonators. *Physical Review A*, 87, **2013**, 053852. DOI: `10.1103/PhysRevA.87.053852` (cited on page 14).

[24] S. Coen, H. G. Randle, T. Sylvestre, and M. Erkintalo. Modeling of octave-spanning Kerr frequency combs using a generalized mean-field Lugiato-Lefever model. *Optics letters*, 38 (1), **2013**, 37–39. URL: `http://www.ncbi.nlm.nih.gov/pubmed/23282830` (cited on pages 14, 16, 17).

[25] M. Haelterman, S. Trillo, and S. Wabnitz. Dissipative modulation instability in a nonlinear dispersive ring cavity. *Optics Communications*, 91 (5-6), **1992**, 401–407. DOI: `10.1016/0030-4018(92)90367-Z` (cited on page 14).

[26] T Hansson, M Bernard, and S Wabnitz. Modulational Instability of Nonlinear Polarization Mode Coupling in Microresonators. 35 (4), **2018**. URL: `https://arxiv.org/pdf/1802.04535.pdf`. arXiv: `arXiv:1802.04535v1` (cited on page 16).

[27] T. Herr, V. Brasch, J. D. Jost, C. Y. Wang, N. M. Kondratiev, M. L. Gorodetsky, and T. J. Kippenberg. Temporal solitons in optical microresonators. *Nature Photonics*, 8 (2), **2014**, 145–152. DOI: `10.1109/CLEOE-IQEC.2013.6801769`. arXiv: `1211.0733` (cited on pages 16, 22, 24).

[28] Y. K. Chembo, I. S. Grudinin, and N Yu. Spatiotemporal dynamics of Kerr-Raman optical frequency combs. *Physical Review A*, 92 (4), **2015**, 4. DOI: `10.1103/PhysRevA.92.043818` (cited on page 16).

[29] C. Godey, I. V. Balakireva, A. Coillet, and Y. K. Chembo. Stability analysis of the spatiotemporal Lugiato-Lefever model for Kerr optical frequency combs in the anomalous and normal dispersion regimes. *Physical Review A*, 89 (6), **2014**, 063814. DOI: `10.1103/PhysRevA.89.063814` (cited on pages 17, 18).

[30] I. V. Barashenkov and Y. S. Smirnov. Existence and stability chart for the ac-driven, damped nonlinear Schrödinger solitons. *Physical Review E - Statistical Physics, Plasmas, Fluids, and Related Interdisciplinary Topics*, 54 (5), **1996**, 5707–5725. DOI: `10.1103/PhysRevE.54.5707` (cited on pages 17, 22).

[31] A Coillet and Y. K. Chembo. Routes to spatiotemporal chaos in Kerr optical frequency combs. *Chaos*, 24 (1), **2014**, 5. DOI: `10.1063/1.4863298`. arXiv: `arXiv:1401.0927v1` (cited on page 19).

[32] L. A. Lugiato and R Lefever. Spatial Dissipative Structures in Passive Optical Systems. *Physical Review Letters*, 58 (21), **1987**, 2209–2211 (cited on page 19).

[33] L. Lugiato and R Lefever. Diffraction stationary patterns in passive optical systems. *Interaction of Radiation with Matter*, **1987** (cited on page 19).

[34] W. H. Renninger and P. T. Rakich. Closed-form solutions and scaling laws for Kerr frequency combs. *Scientific Reports*, 6 (1), **2016**, 24742. DOI: `10.1038/srep24742`. arXiv: `1412.4164` (cited on page 19).

[35] X. Yi, Q.-F. Yang, K. Y. Yang, M.-G. Suh, and K. Vahala. Soliton frequency comb at microwave rates in a high-Q silica microresonator. *Optica*, 2 (12), **2015**, 1078–1085 (cited on pages 22, 24).

[36] S. Coen and M. Erkintalo. Universal scaling laws of Kerr frequency combs. *Optics letters*, 38 (11), **2013**, 1790–1792. DOI: `10.1364/OL.38.001790`. arXiv: `arXiv:1303.7078v1` (cited on page 22).

[37] V. Brasch, T. Herr, M. Geiselmann, G. Lihachev, M. H. P. Pfeiffer, M. L. Gorodetsky, and T. J. Kippenberg. Photonic chip-based optical frequency comb using soliton Cherenkov radiation. *Science*, 351 (6271), **2016**, 357. DOI: `10.1364/CLEO_SI.2015.STh4N.1`. arXiv: `1410.8598` (cited on page 24).

[38] V. E. Lobanov, G. V. Lihachev, N. G. Pavlov, A. V. Cherenkov, T. J. Kippenberg, and M. L. Gorodetsky. Harmonization of chaos into a soliton in Kerr frequency combs. *Optics Express*, 24 (24), **2016**, 27382. DOI: `10.1126/science.aah4243`. arXiv: `1607.08222` (cited on page 24).

[39] J. K. Jang, M. Erkintalo, S. G. Murdoch, and S. Coen. Writing and erasing of temporal cavity solitons by direct phase modulation of the cavity driving field. *Optics Letters*, 40 (20), **2015**, 4755–4758. DOI: `10.1364/OL.40.004755`. arXiv: `1501.05289` (cited on page 24).

[40] J. K. Jang, M. Erkintalo, S. Coen, and S. G. Murdoch. Temporal tweezing of light through the trapping and manipulation of temporal cavity solitons. *Nature Communications*, 6, **2015**, 7370. DOI: `10.1038/ncomms8370`. arXiv: `1410.4836` (cited on pages 24, 26, 28, 30).

[41] Y. Wang, B. Garbin, F. Leo, S. Coen, M. Erkintalo, and S. G. Murdoch. Writing and Erasure of Temporal Cavity Solitons via Intensity Modulation of the Cavity Driving Field. *arXiv*, **2018**, 1802.07428. arXiv: `1802.07428` (cited on pages 24, 28).

[42] H. Taheri, A. A. Eftekhar, K. Wiesenfeld, and A. Adibi. Soliton formation in whispering-gallery-mode resonators via input phase modulation. *IEEE Photonics Journal*, 7 (2), **2015**, 2200309. DOI: `10.1109/JPHOT.2015.2416121` (cited on pages 24, 25, 29).

[43] S. B. Papp, K. Beha, P. Del'Haye, F. Quinlan, H. Lee, K. J. Vahala, and S. A. Diddams. Microresonator frequency comb optical clock. *Optica*, 1 (1), **2014**, 10–14. DOI: `10.1364/OPTICA.1.000010`. arXiv: `1309.3525` (cited on page 24).

[44] D Ceoldo, A Bendahmane, J Fatome, G Millot, T Hansson, D Modotto, S Wabnitz, and B Kilber. Multiple four-wave mixing and Kerr combs in a bichromatically pumped nonlinear fiber ring cavity. *Optics Letters*, 41 (23), **2016**, 5462–5465 (cited on page 28).

[45] H. Lee, T. Chen, J. Li, K. Y. Yang, S. Jeon, O. Painter, and K. J. Vahala. Chemically etched ultrahigh-Q wedge-resonator on a silicon chip. *Nature Photonics*, 6 (6), **2012**, 369–373. DOI: `10.1038/nphoton.2012.109`. arXiv: `1112.2196` (cited on page 28).

[46] J. R. Stone, T. C. Briles, T. E. Drake, D. T. Spencer, D. R. Carlson, S. A. Diddams, and S. B. Papp. Thermal and Nonlinear Dissipative-Soliton Dynamics in Kerr Microresonator Frequency Combs. *arXiv*, **2017**, 1708.08405. URL: `http://arxiv.org/abs/1708.08405`. arXiv: `1708.08405` (cited on page 28).

[47] M. Zajnulina, M. Böhm, D. Bodenmüller, K. Blow, J. C. Boggio, A. Rieznik, and M. Roth. Characteristics and stability of soliton crystals in optical fibres for the purpose of optical frequency comb generation. *Optics Communications*, 393 (November 2016), **2017**, 95–102. DOI: `10.1016/j.optcom.2017.02.035` (cited on page 35).

[48] A. Haboucha, H. Leblond, M. Salhi, A. Komarov, and F. Sanchez. Coherent soliton pattern formation in a fiber laser. *Optics Letters*, 33 (5), **2008**, 524–526. DOI: 10.1364/OL.33.000524 (cited on page 35).

[49] F. Amrani, M. Salhi, P. Grelu, H. Leblond, and F. Sanchez. Universal soliton pattern formations in passively mode-locked fiber lasers. *Optics letters*, 36 (9), **2011**, 1545–1547. DOI: 10.1364/OL.36.001545 (cited on page 35).

[50] A. Haboucha, H. Leblond, M. Salhi, A. Komarov, and F. Sanchez. Analysis of soliton pattern formation in passively mode-locked fiber lasers. *Physical Review A*, 78, **2008**, 043806. DOI: 10.1103/PhysRevA.78.043806 (cited on page 35).

[51] B. A. Malomed, A Schwache, and F Mitschke. Soliton lattice and gas in passive fiber-ring resonators. *Fiber and Integrated Optics*, 17 (4), **1998**, 267–277. DOI: 10.1080/014680398244867 (cited on page 35).

[52] F. Mitschke and A. Schwache. Soliton ensembles in a nonlinear resonator. *Journal of Optics B: Quantum and Semiclassical Optics*, 10 (6), **1998**, 779–788 (cited on page 35).

[53] A. Schwache and F. Mitschke. Properties of an optical soliton gas. *Physical Review E*, 55 (6), **1997**, 7720–7725. DOI: 10.1103/PhysRevE.55.7720 (cited on page 35).

[54] T. Kobayashi, T. Sueta, Y. Cho, and Y. Matsuo. High-repetition-rate optical pulse generator using a Fabry-Perot electro-optic modulator. *Applied Physics Letters*, 21 (8), **1972**, 341–343. DOI: 10.1063/1.1654403 (cited on page 46).

[55] M. Kourogi, K. Nakagawa, and M. Ohtsu. Wide-Span Optical Frequency Comb Generator for. 29 (10), **1993** (cited on page 46).

[56] H. Murata, A. Morimoto, T. Kobayashi, and S. Yamamoto. Optical pulse generation by electrooptic-modulation method and its application to integrated ultrashort pulse generators. *IEEE Journal of Selected Topics in Quantum Electronics*, 6 (6), **2000**, 1325–1331. DOI: 10.1109/2944.902186 (cited on page 46).

[57] T. Sakamoto, T. Kawanishi, and M. Izutsu. frequency comb generation using a Mach – Zehnder. *Optics Letters*, 32 (11), **2007**, 1515–1517 (cited on page 46).

[58] I. Morohashi, T. Sakamoto, H. Sotobayashi, T. Kawanishi, I. Hosako, and M. Tsuchiya. Widely repetition-tunable 200 fs pulse source using a Mach-Zehnder-modulator-based flat comb generator and dispersion-flattened dispersion-decreasing fiber. *Optics letters*, 33 (11), **2008**, 1192–1194. DOI: 10.1364/OL.33.001192 (cited on page 46).

[59] A. Ishizawa, T. Nishikawa, A. Mizutori, H. Takara, S. Aozasa, A. Mori, H. Nakano, A. Takada, and M. Koga. Octave-spanning frequency comb generated by 250 fs pulse train emitted from 25 GHz externally phase-modulated laser diode for carrier-envelope-offset-locking. *Electronics Letters*, 46 (19), **2010**, 1343. DOI: 10.1049/el.2010.2228 (cited on page 46).

[60] R. Wu, V. R. Supradeepa, C. M. Long, D. E. Leaird, and A. M. Weiner. Generation of very flat optical frequency combs from continuous-wave lasers using cascaded intensity and phase modulators driven by tailored radio frequency waveforms. *Optics Letters*, 35 (19), **2010**, 3234. DOI: `10.1364/OL.35.003234`. arXiv: `1005.5373` (cited on page 46).

[61] V. R. Supradeepa and A. M. Weiner. Bandwidth scaling and spectral flatness enhancement of optical frequency combs from phase-modulated continuous-wave lasers using cascaded four-wave mixing. *Optics Letters*, 37 (15), **2012**, 3066. DOI: `10.1364/OL.37.003066` (cited on page 46).

[62] A. J. Metcalf, V. Torres-company, D. E. Leaird, S. Member, A. M. Weiner, and A. Broadband. High-Power Broadly Tunable Electrooptic Frequency Comb Generator. *IEEE Journal of Selected Topics in Quantum Electronics*, 19 (6), **2013**, 3500306. URL: `http://ieeexplore.ieee.org/stamp/stamp.jsp?arnumber=06553388` (cited on page 46).

[63] R. Wu, V. Torres-company, D. E. Leaird, and A. M. Weiner. Optical Frequency Comb Generation. 21 (5), **2013**, 6045–6052. DOI: `10.1364/OE.21.006045` (cited on page 46).

[64] J. M. Dudley, G. G. Genty, and S. Coen. Supercontinuum generation in photonic crystal fiber. *Reviews of Modern Physics*, 78 (4), **2006**, 1135–1184. DOI: `10.1103/RevModPhys.78.1135` (cited on pages 50, 61).

[65] A. M. Weiner. Femtosecond pulse shaping using spatial light modulators. *Review of Scientific Instruments*, 71 (5), **2000**, 1929–1960. DOI: `10.1063/1.1150614` (cited on page 50).

[66] K. Beha, D. C. Cole, P. Del'Haye, A. Coillet, S. A. Diddams, and S. B. Papp. Electronic synthesis of light. *Optica*, 4 (4), **2017**, 406–411. DOI: `10.1364/OPTICA.4.000406` (cited on pages 51, 53, 69).

[67] a. a. Amorim, M. V. Tognetti, P Oliveira, J. L. Silva, L. M. Bernardo, F. X. Kärtner, and H. M. Crespo. Sub-two-cycle pulses by soliton self-compression in highly nonlinear photonic crystal fibers. *Optics letters*, 34 (24), **2009**, 3851–3853. DOI: `10.1364/OL.34.003851` (cited on page 51).

[68] G. Di Domenico, S. Schilt, and P. Thomann. Simple approach to the relation between laser frequency noise and laser line shape. *Applied optics*, 49 (25), **2010**, 4801–4807. DOI: `10.1364/AO.49.004801` (cited on page 53).

[69] S. Backus, C. G. Durfee, M. M. Murnane, and H. C. Kapteyn. High power ultrafast lasers. *Review of Scientific Instruments*, 69 (3), **1998**, 1207. DOI: `10.1063/1.1148795` (cited on page 56).

[70] A. Baltuska, M. Uiberacker, E. Goulielmakis, R. Kienberger, V. S. Yakovlev, T. Udem, T. W. Hänsch, and F. Krausz. Phase-Controlled Amplification of Few-Cycle Laser Pulses. *IEEE Journal of Selected Topics in Quantum Electronics*, 9 (4), **2003**, 972–989 (cited on page 56).

[71] C. Gohle, J. Rauschenberger, T. Fuji, T. Udem, A. Apolonski, F. Krausz, and T. W. Hänsch. Carrier envelope phase noise in stabilized amplifier systems. 30 (18), **2005**, 2487–2489 (cited on pages 56, 63).

[72] J. Rauschenberger, T. Fuji, M. Hentschel, A.-J. Verhoef, T. Udem, C. Gohle, T. W. Hänsch, and F. Krausz. Carrier-envelope phase-stabilized amplifier system. *Laser Physics Letters*, 3 (1), **2006**, 37–42. DOI: `10.1002/lapl.200510053` (cited on page 56).

[73] M. Hirano, T. Nakanishi, T. Okuno, and M. Onishi. Silica-Based Highly Nonlinear Fibers and Their Application. *Sel. Top. Quantum Electron.*, 15 (1), **2009**, 103–113. DOI: `10.1109/JSTQE.2008.2010241` (cited on page 58).

[74] D. Mandridis, I. Ozdur, F. Quinlan, M. Akbulut, J. J. Plant, P. W. Juodawlkis, and P. J. Delfyett. Low-noise, low repetition rate, semiconductor-based mode-locked laser source suitable for high bandwidth photonic analog – digital conversion. *Applied Optics*, 49 (15), **2010**, 2850–2857 (cited on page 61).

[75] D. C. Cole, K. M. Beha, S. A. Diddams, and S. B. Papp. Octave-spanning supercontinuum generation via microwave frequency multiplication. *Proceedings of the 8th Sympsion on Frequency Standards and Metrology 2015, Journal of Physics: Conference Series*, 723, **2016**, 012035. DOI: `10.1088/1742-6596/723/1/012035` (cited on page 64).

[76] A. M. Heidt. Efficient Adaptive Step Size Method for the Simulation of Supercontinuum Generation in Optical Fibers. *Journal of Lightwave Technology*, 27 (18), **2009**, 3984–3991 (cited on page 67).

[77] J. Hult. A Fourth-Order Runge-Kutta in the Interaction Picture Method for Simulating Supercontinuum Generation in Optical Fibers. *Journal of Lightwave Technology*, 25 (12), **2007**, 3770–3775. DOI: `10.1109/JLT.2007.909373` (cited on page 67).

[78] R. Driad, J. Rosenzweig, R. E. Makon, R. Lösch, V. Hurm, H. Walcher, and M. Schlechtweg. InP DHBT-Based IC Technology for 100-Gb / s Ethernet. *IEEE Trans. on Electron. Devices*, 58 (8), **2011**, 2604–2609 (cited on page 69).

[79] D. Ferenci, M. Grozing, M. Berroth, R. Makon, R. Driad, and J. Rosenzweig. A 25 GHz Analog Demultiplexer with a Novel Track and Hold Circuit for a 50 GS / s A / D-Conversion System in InP DHBT Technology. In: **Microwave Symposium Digest**. 2012, pp. 1–3 (cited on page 69).